EFFECT OF INHOMOGENEITY AND UNSTEADINESS ON THE STABILITY OF HIGH-SPEED SHEAR FLOWS

A Dissertation

by

REBECCA LYNNE BERTSCH

Submitted to the Office of Graduate and Professional Studies of
Texas A&M University
in partial fulfillment of the requirements for the degree of

DOCTOR OF PHILOSOPHY

Chair of Committee,	Sharath S. Girimaji
Committee Members,	Rodney D. W. Bowersox
	Diego Donzis
	Prabir Daripa
Head of Department,	Rodney D. W. Bowersox

August 2014

Major Subject: Aerospace Engineering

ABSTRACT

In hypersonic flows, turbulence critically influences mass and momentum transport, mixing, heat transfer and acoustic noise generation. In contrast to incompressible flow, in high speed flows pressure is a true thermodynamic variable and flow-thermodynamic interactions render the investigations extremely challenging. Most studies to date have been performed on steady, uniform or homogeneous shear flows leading to important insight on the flow physics. In most real world applications, flows of practical importance will exhibit unsteadiness and strong inhomogeneity. To date, investigations of unsteadiness and inhomogeneity in high-speed flows are rare. The goal of this dissertation is to study and understand these non-ideal effects when pertinent to shear flows. Towards this goal, we perform three distinct studies: (a) examination of time reversal characteristics of linear inviscid mass, momentum, energy and state equation in compressible flows; (b) Linear analysis (RDT) of compressibility effects on instabilities in temporally periodic (unsteady) homogeneous shear flow; and (c) Numerical investigation of small perturbation evolution in compressible Kolmogorov (inhomogeneous) shear flow.

The first study shows that even with the additional governing equations required in the high-speed regime, the inviscid flow field is still reversible. This justifies the use of temporal periodicity to investigate the effect of unsteadiness. The second study presents a detailed analysis of the pressure equation in temporally periodic homogeneous shear flow. The analysis and numerical results show unsteady uniform shear exhibits two stages of evolution due to the changing behavior of pressure.

These stages are analogous to the first two stages of evolution established in steady shear. The third stage seen in steady shear is not achieved by periodic shear flow. The final study shows that the evolution of small perturbations in spatially periodic Kolmogorov flow is influenced by: i) the initial compressibility parameter, M_{g0}, ii) the initial perturbation orientation, and iii) the stream normal location. Ultimately, the final study supports the postulate that all shear flows exhibit perturbation stability boundary classifications seen in homogeneous shear flows. The findings of this research further our understanding of the effects of unsteadiness and inhomogeneity in realistic flows, which will aid in the development of improved computational tools.

To my family and friends who have always encouraged me to reach for the stars.

ACKNOWLEDGEMENTS

I would like to take this opportunity to thank everyone who supported me during my graduate career and helped me complete my doctoral dissertation. First of all, I would like to thank my graduate advisor, Dr. Sharath Girimaji, for helping me develop the necessary research, presentation and writing skills to build a successful career. His unique teaching ability has aided me in understanding the fundamental concepts of fluid turbulence. I would like to thank Dr. Rodney Bowersox, Dr. Diego Donzis and Dr. Prabir Daripa for their participation on my doctoral committee and giving feedback and suggestions in the dissertation writing process. The courses I took with each of them were vital to completion of my research. I would like to thank the staff of the Aerospace Engineering Department for all their help. I would like to personally thank Karen Knabe for her expertise in the Thesis/Dissertation paperwork deadlines and for always having a warm and welcoming smile.

I would like to thank all the members of Dr. Girimajis research group during my graduate career and special acknowledgement to Dasia, Jacob, Zhimin, Sawan, Gaurav, Carlos and Mona. The weekly turbulence presentations/discussions really improved my understanding of not only my particular research area but the wide range of research that is conducted within our group.

I must acknowledge my family and friends back home in Colorado whose support over the last seven years has meant more to me then they could ever know. There were many times it was incredibly difficult being far away but your emails, phone calls, pictures and videos got me through them.

And finally, to all the amazing friends I met during my graduate career thanks for your unwavering support. My time at Texas A&M would not have been the same without any of you. You all have a special place in my heart.

This work was supported by the NASA and AFOSR grants for the National Center for Hypersonic Laminar-Turbulent Transition Research at Texas A & M University.

TABLE OF CONTENTS

Page

LIST OF FIGURES

LIST OF TABLES

CHAPTER I

INTRODUCTION

Ever since the Wright brothers made the first powered, controlled human flight over a century ago, mankind has sought to fly faster and higher. In recent decades, hypersonic flight is being considered for space access as well as atmospheric transport. Hypersonic flight presents many challenges and opportunities to scientists and engineers. Turbulence is crucial in several aspects of hypersonic flight - mass flow at the intake, heating in the boundary layer, mixing in the combustor and acoustic noise generation are all critically influenced by turbulence. The quintessential element that makes hypersonic flow, and more specifically compressible turbulence, so complex is the change in the nature of pressure. Over the past several years, several investigations have been performed to examine the influence of compressibility in a variety of flows. The goal of these studies is to develop improved closure models and control strategies to predict and control transition and turbulence in different high-speed applications.

In incompressible flows, pressure can be considered a Lagrangian multiplier with the sole purpose of imposing the divergence-free condition. Under these conditions the velocity field is purely solenoidal. However, in high-speed flows pressure is a full-fledged thermodynamic variable evolving according to a wave equation. As a result, the dilatational mode of velocity fluctuations becomes more prominent in high-speed flows. This introduces new energy exchange mechanisms such as pressure dilatation, which is responsible for energy exchange between dilatational and pressure fields. Understanding these thermodynamic-velocity interactions will help develop improved

computational tools for design and development of high-speed flight vehicles.

Studies of high-speed shear flows show that compressibility has a stabilizing effect on the evolution of turbulence. Experiments of high-speed mixing layers observed reduced production rates [1–3]. Computational studies of high-speed homogeneous shear flow performed by Sarkar [4] and Simone et Al. [5] conclude that compressibility has a 'stabilizing' effect on the growth rate of turbulent kinetic energy. This stabilizing effect is found to increase with the gradient Mach number, M_g. More recent studies have identified multiple stages of turbulent kinetic energy evolution [6–8] in compressible homogeneous shear flows and analysis of the pressure equation has pinpointed the onset times of each stage which are functions of M_g [9]. The extensive investigations performed on high-speed homogeneous shear flows and mixing layers has led to the hypothesis that all shear flows exhibit similar qualitative behavior in the compressible regime.

Most of the fundamental analysis and investigations to date address homogeneous and steady shear effects in high-speed flows [9–11]. Practical applications often involve spatial and temporal variations in shear. It is therefore critical to understand the consequences of these 'non-ideal conditions on transition and turbulence in high-speed shear flows. Even in incompressible flows, the effect of unsteady shear is complicated. Girimaji et al [13] and Yu and Girimaji [12] demonstrate that unsteady shear leads to a phase lag between the frequency of the shearing rate and the evolution of the shear anisotropy, b_{12}. The precise degree of phase lag depends on the timescales of perturbation and shear unsteadiness. Some combinations of timescales lead to out-of-phase oscillations between stress and strain resulting in suppression

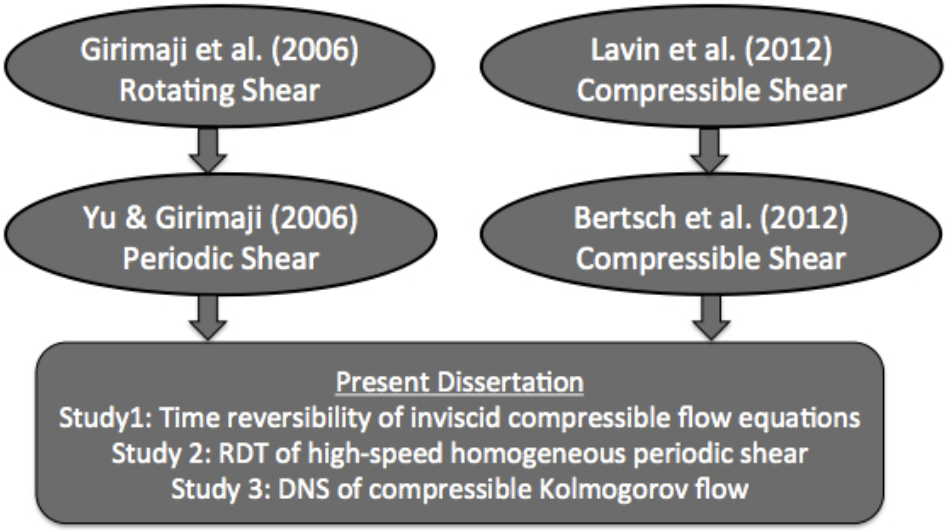

Figure I.1. A schematic of previous studies that paved the way for the studies presented in this dissertation.

of the perturbations. Figure I.1 shows a research roadmap of previous studies and highlights where the studies in this dissertation will improve current understanding of high-speed shear flows by examining combinations of effects.

The objective of this thesis is to examine the effects of shear unsteadiness and inhomogeneity on transition and turbulence in high-speed flows. We perform DNS and RDT studies of spatially and temporally periodic shear flows to build upon our comprehension of the stabilizing effects of compressibility on transition to turbulence. Our main goals are to (a) provide extended validation of the qualitative behavior of all compressible shear flows in respect to pressure evolution and classification of stability boundaries and (b) investigate the effects of inhomogeneity (implemented through a spatially periodic mean flow) and unsteadiness (implemented through a temporally periodic mean flow field) on compressible high-speed shear flows. The

thesis is comprised of three studies:

1. Investigation of the reversibility characteristics of compressible mass, momentum and energy equations.

2. Analysis of implied periodic unsteadiness in the rapid distortion limit of high-speed homogeneous shear flow.

3. Direct numerical simulations (DNS) of the compressible Kolmogorov flow.

A brief introduction to each of the studies is presented next.

I.A. Study 1: Time Reversibility of Compressible Flow Equations

The property of the governing flow equations under time-reversibility transformation is important for inferring the behavior of the system when subject to unsteady forcing. It is well known that incompressible Navier Stokes equations are irreversible solely due to the action of viscosity. However, investigation of the low-speed inviscid Euler equations [14] has shown flow reversal is theoretically permissible under certain conditions. Some studies have attempted to utilize this analysis in order to improve existing modeling approaches [15]. The first short study of this dissertation will apply the time-reversal transformation to high-speed flow equations. The time-reversibility analysis in compressible flow is rendered much more complicated than in incompressible flow due involvement of additional equations - mass conservation, energy balance and thermodynamic state equation.

I.B. Study 2: Rapid Distortion Analysis of Turbulence Subject to High-speed Periodic Shear

The combined effects of compressibility and unsteady (periodic) shear on a high-speed homogeneous turbulence flow field are investigated in the linear rapid distortion limit. In particular, the effect of unsteady shear on flow-thermodynamics interactions is examined. Simplified linear analysis of the perturbation pressure equation reveals crucial differences between steady and unsteady shear effects. The differences are confirmed by numerical simulations of the governing equations at the inviscid rapid distortion theory (RDT) limit. Unlike steadily sheared compressible flows, the unsteady case does not exhibit a final perturbation growth stage. Further, the parametric resonance phenomenon found in incompressible unsteady shear turbulence is absent in the compressible case. Overall, the stabilizing influence of both unsteadiness and compressibility are compounded. The underlying flow mechanisms are investigated and a simple physical explanation is developed.

I.C. Study 3: Direct Numerical Simulations of Compressible Kolmogorov Flow

By construction, Kolmogorov flow features a spatially periodic mean flow. Thus, it incorporates a range of velocity gradients and hence is the archetypal inhomogeneous flow. This flow is of simple geometry and yet provides an ideal test-bed for examining the inhomogeneity effects in low and high-speed applications. In this study, direct numerical simulations of the Kolmogorov flow were performed to investigate the flow physics of individual perturbation modes as well as that of a collection

of isotropically distributed modes. It is demonstrated that the behavior of pressure, and consequently the evolution of the flow field, is dependent on three factors: (i) the initial Mach number at the maximum shear plane, (ii) the initial orientation of the perturbation wave in the shear plane, and (iii) the magnitude of effective Mach number at different vertical planes. The degree of stabilization, if any, compared to an equivalent homogeneous shear flow is quantified. The difference between streamwise and spanwise perturbations is examined. The evolution of dilatational fluctuations as a function of initial orientation is examined. The stability characteristics as a function of initial orientation are established. Comparing the stability characteristics at different locations of shear levels isolates the inhomogeneity effect. Overall, this study presents a clear analysis that shows the stabilizing influence of compressibility is somewhat modified by mean shear inhomogeneity, but the fundamental characteristics remain.

In summary, the different studies performed in this dissertation seek to clearly isolate the influences of unsteadiness and inhomogeneity in high-speed shear flows. In the subsequent chapters each of the three studies are presented in detail. The summary of the dissertation findings is presented in the Conclusion section.

CHAPTER II

TIME REVERSIBILITY IN LINEAR, INVISCID FLOWS: LOW-SPEED VS HIGH-SPEED

This chapter will serve as a prelude to the extensive analysis in Chapter III that will examine the influence of forced periodic unsteadiness on a compressible uniform shear flow. The time reversibility characteristics of the low speed Euler equations have been established and studied [14, 15] for its implications in modeling. However, analysis of time reversibility in high-speed flows, where pressure is governed by state and energy equations instead of Poisson's equation, needs to be performed. In this chapter, full analysis of time reversibility in the inviscid, Navier-Stokes equations will be presented for both low-speed and high-speed flows highlighting the key differences. The final section of this chapter will discuss implications of the effects of unsteadiness in high-speed shear flows.

II.A. Low-speed Governing Equations

The analysis for the low-speed or incompressible regime begins with the instantaneous mass, momentum, Poisson and wave vector evolution equations:

$$\frac{\partial \rho}{\partial t} + \frac{\partial (\rho u_j)}{\partial x_j} = 0 \quad \rightarrow \quad \nabla \cdot \vec{u} = 0 \tag{2.1}$$

$$\frac{\partial u_i}{\partial t} + u_j \frac{\partial u_i}{\partial x_j} = -\frac{1}{\rho}\frac{\partial p}{\partial x_i} + \nu \frac{\partial^2 u_i}{\partial x_j \partial x_j} \tag{2.2}$$

$$\nabla^2 p = -\rho \left(\frac{\partial u_i}{\partial x_j} \frac{\partial u_j}{\partial x_i} \right) \tag{2.3}$$

We commence the derivation with a decomposition of the flow field variables.

The variables are decomposed into their mean/background component (denoted by $\overline{f}$) and their fluctuation/perturbation component (denoted by $(f^{'})$):

$$\rho = \overline{\rho} + \rho^{'}, \quad U_i = \overline{U_i} + u_i^{'}, \quad p = \overline{p} + p^{'}. \tag{2.4}$$

Substituting the expansion into the equations leads to:

$$\frac{\partial(\overline{U}_i + u_i')}{\partial t} + (\overline{U}_j + u_j')\frac{\partial(\overline{U}_i + u_i')}{\partial x_j} = -\frac{1}{(\overline{\rho} + \rho')}\frac{\partial(\overline{p} + p')}{\partial x_i}, \tag{2.5}$$

$$\nabla^2(\overline{p} + p') = -(\overline{\rho} + \rho')\frac{\partial(\overline{U}_i + u_i')}{\partial x_j}\frac{\partial(\overline{U}_j + u_j')}{\partial x_i}. \tag{2.6}$$

We subject the instantaneous equations (2.5 and 2.6) to averaging to construct the mean/background field governing equations:

$$\frac{\partial \overline{U}_i}{\partial t} + \overline{U}_j\frac{\partial \overline{U}_i}{\partial x_j} = -\frac{1}{\overline{\rho}}\frac{\partial \overline{p}}{\partial x_i} + \overline{\frac{\rho'}{(\overline{\rho})^2}\frac{\partial p'}{\partial x_i}} - \overline{u_j'\frac{\partial u_i'}{\partial x_j}}, \tag{2.7}$$

$$\nabla^2\overline{p} = -\overline{\rho}\left(\frac{\partial \overline{U}_i}{\partial x_j}\frac{\partial \overline{U}_j}{\partial x_i} + \overline{\frac{\partial u_i'}{\partial x_j}\frac{\partial u_j'}{\partial x_i}}\right) - 2\overline{\rho'\frac{\partial u_i'}{\partial x_j}}\frac{\partial \overline{U}_j}{\partial x_i}. \tag{2.8}$$

The mean field equations (2.7 and 2.8) are subtracted from the instantaneous decomposed field equations (2.5 and 2.6) to reveal the governing equations for the perturbation/fluctuation field:

$$\begin{aligned}\frac{\partial u_i'}{\partial t} + \overline{U}_j\frac{\partial u_i'}{\partial x_j} = &- \frac{1}{\overline{\rho}}\frac{\partial p'}{\partial x_i} + \frac{\rho'}{(\overline{\rho})^2}\frac{\partial \overline{p}}{\partial x_i} + \frac{\rho'}{(\overline{\rho})^2}\frac{\partial p'}{\partial x_i} - \overline{\frac{\rho'}{(\overline{\rho})^2}\frac{\partial p'}{\partial x_i}} \\ &- u_j'\frac{\partial \overline{U}_i}{\partial x_j} - u_j'\frac{\partial u_i'}{\partial x_j} + \overline{u_j'\frac{\partial u_i'}{\partial x_j}},\end{aligned} \tag{2.9}$$

$$\begin{aligned}\nabla^2 p' = &- \overline{\rho}\left(\frac{\partial \overline{U}_i}{\partial x_j}\frac{\partial u_j'}{\partial x_i} + \frac{\partial u_i'}{\partial x_j}\frac{\partial \overline{U}_j}{\partial x_i} - + \frac{\partial u_i'}{\partial x_j}\frac{\partial u_j'}{\partial x_i} - \overline{\frac{\partial u_i'}{\partial x_j}\frac{\partial u_j'}{\partial x_i}}\right) \\ &- \rho'\left(\frac{\partial \overline{U}_i}{\partial x_j}\frac{\partial \overline{U}_j}{\partial x_i} + \frac{\partial \overline{U}_i}{\partial x_j}\frac{\partial u_j'}{\partial x_i} - \frac{\partial u_i'}{\partial x_j}\frac{\partial \overline{U}_j}{\partial x_i} - \frac{\partial u_i'}{\partial x_j}\frac{\partial u_j'}{\partial x_i} + \overline{\frac{\partial u_i'}{\partial x_j}\frac{\partial u_j'}{\partial x_i}}\right) \\ &+ 2\overline{\rho'\frac{\partial u_i'}{\partial x_j}}\frac{\partial \overline{U}_j}{\partial x_i} + H.O.T.\end{aligned} \tag{2.10}$$

Now we reduce the governing equations to their linearized form. All terms that are higher than first order in perturbation/fluctuation variables are neglected:

$$\frac{\partial u_i'}{\partial t} + \overline{U}_j \frac{\partial u_i'}{\partial x_j} = -\frac{1}{\overline{\rho}} \frac{\partial p'}{\partial x_i} + \frac{\rho'}{(\overline{\rho})^2} \frac{\partial \overline{p}}{\partial x_i} - u_j' \frac{\partial \overline{U}_i}{\partial x_j} \tag{2.11}$$

$$\nabla^2 p' = -2\overline{\rho} \frac{\partial \overline{U}_i}{\partial x_j} \frac{\partial u_j'}{\partial x_i} - \rho' \frac{\partial \overline{U}_i}{\partial x_j} \frac{\partial \overline{U}_j}{\partial x_i} \tag{2.12}$$

Next, we restrict our attention to a homogeneous mean flow field. The homogeneous condition implies that the mean velocity gradient and thermodynamic variables are uniform throughout the spatial domain leading to:

$$\frac{\partial \overline{P}}{\partial x_i} = \frac{\partial \overline{\rho}}{\partial x_i} = 0, \tag{2.13}$$

$$\frac{\partial \overline{U}_i}{\partial x_j}(\vec{x}, t) = \frac{\partial \overline{U}_i}{\partial x_j}(t), \tag{2.14}$$

where $i \neq j$. Applying these assumptions the linear fluctuating equations become:

$$\frac{\partial u_i'}{\partial t} + \overline{U}_j \frac{\partial u_i'}{\partial x_j} = \frac{du_i'}{dt} = -\frac{1}{\overline{\rho}} \frac{\partial p'}{\partial x_i} - u_j' \frac{\partial \overline{U}_i}{\partial x_j} \tag{2.15}$$

$$\nabla^2 p' = -2\overline{\rho} \frac{\partial \overline{U}_i}{\partial x_j} \frac{\partial u_j'}{\partial x_i} \tag{2.16}$$

Using the homogeneity assumption permits us to transform the governing equations into spectral space via Fourier transforms of the flow field variable:

$$\overrightarrow{u}'(\overrightarrow{x}, t) = \sum \hat{\overrightarrow{u}}(t) e^{i\overrightarrow{\kappa}(t)\cdot\overrightarrow{x}}, \rho'(\overrightarrow{x}, t) = \sum \hat{\rho}(t) e^{i\overrightarrow{\kappa}(t)\cdot\overrightarrow{x}}, p'(\overrightarrow{x}, t) = \sum \hat{p}(t) e^{i\overrightarrow{\kappa}(t)\cdot\overrightarrow{x}}, \tag{2.17}$$

where $\vec{\kappa}$ is the wave number vector. This step transforms the set of partial differential equations (PDEs) in physical space to a set of ordinary differential equations (ODEs) in spectral space:

$$\frac{d\hat{u}_i}{dt} = -\frac{i}{\overline{\rho}} \kappa_i \hat{p} - \hat{u}_j S_{ij}, \tag{2.18}$$

$$\hat{p} = -2\overline{\rho}\frac{i\kappa_i}{\kappa^2}\hat{u}_j S_{ij}. \tag{2.19}$$

In this linearized, spectral form, equation (2.19) can be plugged into equation (2.18) to get reduce the set of equations that govern the flow field:

$$\frac{d\hat{u}_i}{dt} = -\frac{i}{\overline{\rho}}\kappa_i(-2\overline{\rho}\frac{i\kappa_l}{\kappa^2}\hat{u}_j S_{lj}) - \hat{u}_j S_{ij}. \tag{2.20}$$

$$\frac{d\kappa_i}{dt} = -\kappa_j\frac{\partial U_i}{\partial x_j} \tag{2.21}$$

With the governing equations in this form, we perform the following transformations [44]:

$$t = \tilde{t}; \quad u_j = -\tilde{u}_j; \quad S_{ij} = -\tilde{S}_{ij}. \tag{2.22}$$

Applying these transformations to (2.25) and the wave-vector evolution equation (2.24):

$$\frac{d(-\tilde{\hat{u}}_i)}{dt} = -\frac{i}{\overline{\rho}}\kappa_i(-2\overline{\rho}\frac{i\kappa_l}{\kappa^2}(-\tilde{\hat{u}}_j)(-\tilde{S}_{lj})) - (-\tilde{\hat{u}}_j)(-\tilde{S}_{ij}), \tag{2.23}$$

$$\frac{d\kappa_i}{dt} = -\kappa_j(-\tilde{S}_{ji}), \tag{2.24}$$

which reduces to:

$$\frac{d\tilde{\hat{u}}_i}{dt} = -\left(-\frac{i}{\overline{\rho}}\kappa_i(-2\overline{\rho}\frac{i\kappa_l}{\kappa^2}\tilde{\hat{u}}_j\tilde{S}_{lj}) - \tilde{\hat{u}}_j\tilde{S}_{ij}\right) = -\frac{d\hat{u}_i}{dt}, \tag{2.25}$$

$$\frac{d\tilde{\kappa}_i}{dt} = -\left(-\kappa_j\tilde{S}_{ji}\right) = -\frac{d\kappa_i}{dt}. \tag{2.26}$$

Thus, we recover the well known result that the inviscid perturbation equations are fully reversible in incompressible flows. Several studies have examined the implications of time reversibility of the Euler equations for developing closure models. The purpose of the low-speed derivation here is to set up the ground work for comparison with the high-speed derivation that follows.

II.B. High-speed Governing Equations

For high-speed flows, we begin with the conservation equations for mass momentum, and energy along with the ideal gas law:

$$\frac{\partial \rho}{\partial t} + \frac{\partial (\rho u_j)}{\partial x_j} = 0, \tag{2.27}$$

$$\frac{\partial (\rho u_i)}{\partial t} + \frac{\partial (\rho u_i u_j)}{\partial x_j} = -\frac{\partial p}{\partial x_i} + \mu \frac{\partial^2 u_i}{\partial x_j \partial x_j}, \tag{2.28}$$

$$\frac{\partial (\rho T)}{\partial t} + \frac{\partial (\rho T u_j)}{\partial x_j} = -\frac{p}{c_v} \frac{\partial u_j}{\partial x_j}, \tag{2.29}$$

$$p = \rho R T. \tag{2.30}$$

Once again, we restrict our consideration to inviscid ideal gas flow. The momentum equation can be written as:

$$\frac{\partial \rho}{\partial t} + u_j \frac{\partial \rho}{\partial x_j} = -\rho \frac{\partial u_j}{\partial x_j}, \tag{2.31}$$

$$\frac{\partial u_i}{\partial t} + u_j \frac{\partial u_i}{\partial x_j} = -\frac{\partial p}{\partial x_i}, \tag{2.32}$$

$$\frac{\partial p}{\partial t} + u_j \frac{\partial p}{\partial x_j} = -\gamma p \frac{\partial u_j}{\partial x_j}. \tag{2.33}$$

We decompose the field into the mean/background and fluctuation/perturbation parts in the same manner as the low-speed case:

$$\frac{\partial (\overline{\rho} + \rho')}{\partial t} + (\overline{u}_j + u'_j) \frac{\partial (\overline{\rho} + \rho')}{\partial x_j} = -(\overline{\rho} + \rho') \frac{\partial (\overline{u}_j + u'_j)}{\partial x_j}, \tag{2.34}$$

$$\frac{\partial (\overline{U}_i + u'_i)}{\partial t} + (\overline{U}_j + u'_j) \frac{\partial (\overline{U}_i + u'_i)}{\partial x_j} = -\frac{1}{(\overline{\rho} + \rho')} \frac{\partial (\overline{p} + p')}{\partial x_i}, \tag{2.35}$$

$$\frac{\partial (\overline{p} + p')}{\partial t} + (\overline{U}_j + u'_j) \frac{\partial (\overline{p} + p')}{\partial x_j} = -\gamma (\overline{p} + p') \frac{\partial (\overline{U}_j + u'_j)}{\partial x_j}. \tag{2.36}$$

Reynolds averaging applied to the high-speed field equations leading to the mean/background governing equations:

$$\frac{\partial \overline{\rho}}{\partial t} + \overline{U}_j \frac{\partial \overline{\rho}}{\partial x_j} = -\overline{\rho}\frac{\partial \overline{U}_j}{\partial x_j} - \overline{u'_j \frac{\partial \rho'}{\partial x_j}} - \overline{\rho' \frac{\partial u'_j}{\partial x_j}}, \tag{2.37}$$

$$\frac{\partial \overline{U}_i}{\partial t} + \overline{U}_j \frac{\partial \overline{U}_i}{\partial x_j} = -\frac{1}{\overline{\rho}}\frac{\partial \overline{p}}{\partial x_i} + \overline{\frac{\rho'}{(\overline{\rho})^2}\frac{\partial p'}{\partial x_i}} - \overline{u'_j \frac{\partial u'_i}{\partial x_j}}, \tag{2.38}$$

$$\frac{\partial \overline{p}}{\partial t} + \overline{U}_j \frac{\partial \overline{p}}{\partial x_j} = -\gamma\overline{p}\frac{\partial \overline{U}_j}{\partial x_j} - \gamma\overline{p' \frac{\partial u'_j}{\partial x_j}} - \overline{u'_j \frac{\partial p'}{\partial x_j}}. \tag{2.39}$$

Subtracting the mean field equations (2.37-2.39) from the instantaneous field equations (2.34-2.36) reveals the fluctuating field equations:

$$\frac{\partial \rho'}{\partial t} + \overline{U}_j \frac{\partial \rho'}{\partial x_j} = -u'_j \frac{\partial \overline{\rho}}{\partial x_j} - \rho' \frac{\partial \overline{U}_j}{\partial x_j} - \overline{\rho}\frac{\partial u'_j}{\partial x_j} - u'_j \frac{\partial \rho'}{\partial x_j} - \rho' \frac{\partial u'_j}{\partial x_j} + \overline{u'_j \frac{\partial \rho'}{\partial x_j}} + \overline{\rho' \frac{\partial u'_j}{\partial x_j}}, \tag{2.40}$$

$$\begin{aligned} \frac{\partial u'_i}{\partial t} + \overline{U}_j \frac{\partial u'_i}{\partial x_j} = & - \frac{1}{\overline{\rho}}\frac{\partial p'}{\partial x_i} + \frac{\rho'}{(\overline{\rho})^2}\frac{\partial \overline{p}}{\partial x_i} + \frac{\rho'}{(\overline{\rho})^2}\frac{\partial p'}{\partial x_i} - \overline{\frac{\rho'}{(\overline{\rho})^2}\frac{\partial p'}{\partial x_i}} \\ & - u'_j \frac{\partial \overline{U}_i}{\partial x_j} - u'_j \frac{\partial u'_i}{\partial x_j} + \overline{u'_j \frac{\partial u'_i}{\partial x_j}}, \end{aligned} \tag{2.41}$$

$$\frac{\partial p'}{\partial t} + \overline{U}_j \frac{\partial p'}{\partial x_j} = -\gamma\overline{p}\frac{\partial u'_j}{\partial x_j} - \gamma p' \frac{\partial \overline{U}'_j}{\partial x_j} - u'_j \frac{\partial \overline{p}}{\partial x_j} - \gamma p' \frac{\partial u'_j}{\partial x_j} + \gamma\overline{p' \frac{\partial u'_j}{\partial x_j}} - u'_j \frac{\partial p'}{\partial x_j} + \overline{u'_j \frac{\partial p'}{\partial x_j}}. \tag{2.42}$$

The linearized fluctuation equations are:

$$\frac{\partial \rho'}{\partial t} + \overline{U}_j \frac{\partial \rho'}{\partial x_j} = -\rho' \frac{\partial \overline{U}_j}{\partial x_j} - + u'_j \frac{\partial \overline{\rho}}{\partial x_j} - \overline{\rho}\frac{\partial u'_j}{\partial x_j}, \tag{2.43}$$

$$\frac{\partial u'_i}{\partial t} + \overline{U}_j \frac{\partial u'_i}{\partial x_j} = -\frac{1}{\overline{\rho}}\frac{\partial p'}{\partial x_i} + \frac{\rho'}{(\overline{\rho})^2}\frac{\partial \overline{p}}{\partial x_i} - u'_j \frac{\partial \overline{U}_i}{\partial x_j}, \tag{2.44}$$

$$\frac{\partial p'}{\partial t} + \overline{U}_j \frac{\partial (p')}{\partial x_j} = -\gamma p' \frac{\partial \overline{U}_j}{\partial x_j} - \gamma\overline{p}\frac{\partial u'_j}{\partial x_j} - u'_j \frac{\partial \overline{p}}{\partial x_j}. \tag{2.45}$$

For a homogeneous shear flow this reduces to:

$$\frac{\partial \rho'}{\partial t} + \overline{U}_j \frac{\partial \rho'}{\partial x_j} = \frac{d\rho'}{dt} = -\overline{\rho}\frac{\partial u'_j}{\partial x_j}, \tag{2.46}$$

$$\frac{\partial u'_i}{\partial t} + \overline{U}_j \frac{\partial u'_i}{\partial x_j} = \frac{du'_i}{dt} = -\frac{1}{\overline{\rho}}\frac{\partial p'}{\partial x_i} - u'_j \frac{\partial \overline{U}_i}{\partial x_j}, \tag{2.47}$$

$$\frac{\partial p'}{\partial t} + \overline{U}_j \frac{\partial p'}{\partial x_j} = \frac{dp'}{dt} = -\gamma\overline{p}\frac{\partial u'_j}{\partial x_j}. \tag{2.48}$$

Transforming the linear, fluctuating field equations to spectral space, the set of PDEs become ODEs:

$$\frac{d\hat{\rho}}{dt} = -i\overline{\rho}\kappa_j\hat{u}_j, \tag{2.49}$$

$$\frac{d\hat{u}_i}{dt} = -\frac{i}{\overline{\rho}}\kappa_i\hat{p} - \hat{u}_j S_{ij}, \tag{2.50}$$

$$\frac{d\hat{p}}{dt} = -i\gamma\overline{p}\kappa_j\hat{u}_j. \tag{2.51}$$

This is the final form of the high-speed inviscid governing equations. The wave vector evolution equation remains unaltered from the low-speed limit (2.24). It is important to note that unlike the low-speed case where the momentum equation is independent of the mass and energy equations, here all the equations are interconnected.

Applying the time reversibility transformations (2.22) to the high-speed equations:

$$\frac{d\hat{\rho}}{dt} = -i\overline{\rho}\kappa_j(-\tilde{\hat{u}}_j), \tag{2.52}$$

$$\frac{d(-\tilde{\hat{u}}_i)}{dt} = -\frac{i}{\overline{\rho}}\kappa_i\hat{p} - (-\tilde{\hat{u}}_j)(-\tilde{S}_{ij}), \tag{2.53}$$

$$\frac{d\hat{p}}{dt} = -i\gamma\overline{p}\kappa_j(-\tilde{\hat{u}}_j), \tag{2.54}$$

which reduces to:

$$\frac{d\tilde{\hat{\rho}}}{dt} = -(-i\overline{\rho}\kappa_j\tilde{\hat{u}}_j) = -\frac{d\hat{\rho}}{dt}, \tag{2.55}$$

$$\frac{d\tilde{\hat{u}}_i}{dt} = -(-\frac{i}{\overline{\rho}}\kappa_i\hat{p} - \tilde{\hat{u}}_j\tilde{S}_{ij}) = -\frac{d\hat{u}_i}{dt}, \tag{2.56}$$

$$\frac{d\tilde{\hat{p}}}{dt} = -(-i\gamma\overline{p}\kappa_j\tilde{\hat{u}}_j) = -\frac{d\hat{p}}{dt}. \tag{2.57}$$

Evidently, the high-speed inviscid linear equations are time reversible, even with the added complexity of compressibility, which has a strong influence on the behavior of pressure.

II.C. Implications for Unsteady Flows

With the knowledge that the linear inviscid equations for both low-speed and high-speed flows analytically show flow field reversibility is possible, we deduce what this will imply for studies examining unsteady flow. Since time reversibility of a flow requires the flow field variables return to their initial state, this concept can be considered highly stabilizing when considering transition to turbulence. Most real world applications will never actually exhibit an instant reversal of all flow field velocities like that theorized in time reversal. However, almost all flow types experience some level of unsteadiness. To gain insight on the overall effects of unsteadiness, it is possible to implement rapid velocity changes in flow fields through use of unsteady forcing in numerical methods or experiments. This concept has been tested in low speed shear flows [12, 13] where a strong suppression of the initial perturbations was witnessed. In the chapter that follows, we will utilize this knowledge of time reversibility in high-speed shear flows to simulate a temporally periodic forcing mechanism on a compressible homogeneous shear flow hypothesizing that a similar form of flow field stabilizing action will occur.

CHAPTER III

RAPID DISTORTION ANALYSIS OF HIGH SPEED HOMOGENOUS TURBULENCE SUBJECT TO PERIODIC SHEAR

III.A. Rapid Distortion Theory of Periodic Compressible Flows

To derive the inviscid RDT equations for an ideal gas, we begin with the instantaneous conservation of mass, momentum and energy equations [16].

$$\frac{\partial \rho}{\partial t} + U_j \frac{\partial \rho}{\partial x_j} = -\rho \frac{\partial U_j}{\partial x_j}, \tag{3.1}$$

$$\frac{\partial U_i}{\partial t} + U_j \frac{\partial U_i}{\partial x_j} = -\frac{1}{\rho} \frac{\partial P}{\partial x_i}, \tag{3.2}$$

$$\frac{\partial T}{\partial t} + U_j \frac{\partial T}{\partial x_j} = -(\gamma - 1) T \frac{\partial U_j}{\partial x_j}, \tag{3.3}$$

$$P = \rho R T. \tag{3.4}$$

Here ρ, U, T, P and γ represent the instantaneous density, velocity, temperature, pressure and the ratio of specific heats. The variables t and x denote temporal and spatial coordinates.

The instantaneous variables are expanded into their Reynolds-averaged (denoted by $(\bar{.})$) and fluctuating parts (denoted by $(.')$): $\rho = \overline{\rho} + \rho'$, $U_i = \overline{U_i} + u_i{}'$, $T = \overline{T} + T'$ and $P = \overline{P} + p'$. By subjecting the instantaneous equations to Reynolds averaging, the governing equations of the mean field quantities are obtained:

$$\frac{\partial \overline{\rho}}{\partial t} + \overline{U_j} \frac{\partial \overline{\rho}}{\partial x_j} = -\overline{\rho} \frac{\partial \overline{U_j}}{\partial x_j} - \frac{\partial \overline{\rho' u_j{}'}}{\partial x_j}, \tag{3.5}$$

$$\frac{\partial \overline{U_j}}{\partial t} + \overline{U_j} \frac{\partial \overline{U_i}}{\partial x_j} + \overline{u_j{}' \frac{\partial u_i{}'}{\partial x_j}} = -\frac{1}{\overline{\rho}} \frac{\partial \overline{P}}{\partial x_i} + \frac{1}{(\overline{\rho})^2} \overline{\rho' \frac{\partial P'}{\partial x_i}} - \frac{\overline{(\rho')^2}}{(\overline{\rho})^3} \frac{\partial \overline{P}}{\partial x_i}, \tag{3.6}$$

$$\frac{\partial \overline{T}}{\partial t} + \overline{U_j}\frac{\partial \overline{T}}{\partial x_j} + \overline{u_j{}'\frac{\partial T'}{\partial x_j}} = -(\gamma-1)\overline{T}\frac{\partial \overline{U_j}}{\partial x_j} - (\gamma-1)\overline{T'\frac{\partial u_j{}'}{\partial x_j}}, \tag{3.7}$$

$$\overline{P} = R\overline{\rho}\overline{T} + R\overline{\rho' T'}. \tag{3.8}$$

The mean field set of equations (3.5 -3.8) are subtracted from the instantaneous set (3.1-3.4) to obtain the fluctuating field equations, which results in the following system of equations:

$$\begin{aligned}\frac{\partial \rho'}{\partial t} + \overline{U_k}\frac{\partial \rho'}{\partial x_k} = &- u_k{}'\frac{\partial \overline{\rho}}{\partial x_k} - u_k{}'\frac{\partial \rho'}{\partial x_k} + \overline{u_k{}'\frac{\partial \rho'}{\partial x_k}} - \overline{\rho}\frac{\partial u_k{}'}{\partial x_k} \\ &- \rho'\frac{\partial \overline{U_k}}{\partial x_k} - \rho'\frac{\partial u_k{}'}{\partial x_k} + \overline{\rho'\frac{\partial u_k{}'}{\partial x_k}},\end{aligned} \tag{3.9}$$

$$\begin{aligned}\frac{\partial u_i{}'}{\partial t} + \overline{U_k}\frac{\partial u_i{}'}{\partial x_k} = &- u_k{}'\frac{\partial \overline{U_i}}{\partial x_k} - u_k{}'\frac{\partial u_i{}'}{\partial x_k} + \overline{u_k{}'\frac{\partial u_i{}'}{\partial x_k}} \\ &+ \frac{\rho'}{(\overline{\rho})^2}\frac{\partial \overline{P}}{\partial x_i} - \frac{(\rho')^2}{(\overline{\rho})^3}\frac{\partial \overline{P}}{\partial x_i} + \frac{\overline{(\rho')^2}}{(\overline{\rho})^3}\frac{\partial \overline{P}}{\partial x_i} \\ &- \frac{R}{(\overline{\rho})^2}\overline{\rho'(\frac{\partial \overline{\rho}T'}{\partial x_i} + \frac{\partial \rho'\overline{T}}{\partial x_i})} \\ &- \frac{R}{\overline{\rho}}\frac{\partial}{\partial x_i}(\overline{\rho}T' + \rho'\overline{T} + \rho'T' - \overline{\rho'T'}) \\ &+ \frac{R\rho'}{(\overline{\rho})^2}\frac{\partial}{\partial x_i}(\overline{\rho}T' + \rho'\overline{T}),\end{aligned} \tag{3.10}$$

$$\begin{aligned}\frac{\partial T'}{\partial t} + \overline{U_k}\frac{\partial T'}{\partial x_k} &= -u_k{}'\frac{\partial \overline{T}}{\partial x_k} - u_k{}'\frac{\partial T'}{\partial x_k} + \overline{u_k{}'\frac{\partial T'}{\partial x_k}} \\ &- (\gamma-1)\overline{T}\frac{\partial u_k{}'}{\partial x_k} - (\gamma-1)T'\frac{\partial \overline{U_k}}{\partial x_k} \\ &- (\gamma-1)T'\frac{\partial u_k{}'}{\partial x_k} + (\gamma-1)\overline{T'\frac{\partial u_k{}'}{\partial x_k}}.\end{aligned} \tag{3.11}$$

At the RDT limit, which focuses on the linear interaction between mean and fluctuating fields, the terms nonlinear in perturbation quantities are neglected. In

this work, we examine a temporally periodic homogeneous shear flow:

$$\frac{\partial \overline{U_i}}{\partial x_j} = \begin{bmatrix} 0 & S_0 cos(\omega t) & 0 \\ 0 & 0 & 0 \\ 0 & 0 & 0 \end{bmatrix}. \tag{3.12}$$

In such a flow, it can be shown that:

$$\overline{\rho}(t) = \overline{\rho}(0); \quad \overline{T}(t) = \overline{T}(0); \quad \overline{p}(t) = \overline{p}(0), \tag{3.13}$$

at the linear limit, which infers that the mean field variables do not evolve beyond their initial values. The fluctuating field equations simplify to [6, 7, 9, 16]:

$$\frac{d\rho'}{dt} = -\overline{\rho}\frac{\partial {u_k}'}{\partial x_k}, \tag{3.14}$$

$$\frac{d{u_i}'}{dt} = -{u_k}'\frac{\partial \overline{U_i}}{\partial x_k} - R\frac{\partial T'}{\partial x_i} - \frac{R\overline{T}}{\overline{\rho}}\frac{\partial \rho'}{\partial x_i}, \tag{3.15}$$

$$\frac{dp'}{dt} = -\gamma\overline{p}\frac{\partial {u_k}'}{\partial x_k}. \tag{3.16}$$

Fourier transforms are applied to the fluctuating governing equations as in the uniform RDT approach:

$$\begin{aligned} {u_i}'(\overrightarrow{x}, t) &= \sum \hat{u_i}(t) e^{i\overrightarrow{\kappa}(t)\cdot\overrightarrow{x}}, \\ \rho'(\overrightarrow{x}, t) &= \sum \hat{\rho}(t) e^{i\overrightarrow{\kappa}(t)\cdot\overrightarrow{x}}, \\ p'(\overrightarrow{x}, t) &= \sum \hat{p}(t) e^{i\overrightarrow{\kappa}(t)\cdot\overrightarrow{x}} \end{aligned} \tag{3.17}$$

where $\overrightarrow{\kappa}$ is the wavenumber vector and $\hat{u_i}$, $\hat{\rho}$, and $\hat{p}$ are the Fourier amplitudes of velocity, density and pressure fluctuations. The RDT equations in spectral space are

given by [10]:

$$\frac{d\hat{\rho}}{dt} = -i\overline{\rho}\ \hat{u}_j\kappa_j, \tag{3.18}$$

$$\frac{d\hat{u}_i}{dt} = -\frac{i}{\overline{\rho}}\hat{p}\kappa_i - \hat{u}_j S_{ij}, \tag{3.19}$$

$$\frac{d\hat{p}}{dt} = -i\gamma\overline{p}\hat{u}_j\kappa_k. \tag{3.20}$$

The components of a wavenumber vector evolve as:

$$\frac{d\kappa_i}{dt} + \kappa_k\frac{\partial\overline{U_k}}{\partial x_i} = 0. \tag{3.21}$$

Equations (3.18-3.21) are now solved numerically employing the particle representation method of Kassinos and Reynolds [17]. This method of solution constructs the governing equations of the required Fourier covariances directly. These covariances represent the moments conditioned upon given wavenumber vectors. Similar equations for steady high-speed homogeneous shear flow were presented in detail by Yu & Girimaji [16] and Lavin [18]. The final set of equations for the simulations consist of 26 ordinary differential equations (ODE).

The initial gradient Mach number, based on an integral length scale, has been recognized as a relevant compressibility parameter in DNS [4] and RDT [9] studies of steady homogeneous shear flows:

$$M_g \equiv \frac{S_0 L}{a}, \tag{3.22}$$

where S_0 is the initial mean velocity gradient ($S \equiv \frac{\partial U_1}{\partial x_2}$) and L is an integral length-scale. The quantity a represents speed of sound based on mean temperature. The relevant length scale in an RDT analysis is one that is distinctive of the mode under consideration. This length scale is inversely proportional to the magnitude of modal

wavenumber, so a relevant Mach number for RDT analysis is given by [10]:

$$M_m \equiv \frac{S_0}{a\|\kappa\|}, \tag{3.23}$$

where $\|\kappa\|$ represents a norm of the wavenumbers under consideration. The modal Mach number (M_m) is a direct measure of the relative significance of pressure effects to inertial effects in the Fourier-transformed fluctuating momentum equation.

III.A.1. Numerical approach

We employed a high-fidelity fourth-order Runge-Kutta scheme to solve the RDT equations. Each simulation is implemented with an incompressible and statistically isotropic initial velocity field. Initial conditions for the wavenumber vector and 25 covariances are specified in Fourier space. More details of the initial field setup can be found in Yu et al. [16], Lavin et al. [10] and Girimaji et al. [19]. The wavenumber $\overrightarrow{\kappa}(t=0)$ and corresponding velocity covariance $< \hat{u}_i \hat{u}_j^* | \overrightarrow{\kappa} >$ are chosen by first distributing the wavenumber vectors uniformly on a unit sphere to render a statistically isotropic initial field. Next, the velocity vectors are selected to be perpendicular to their respective wavenumber vector to ensure an initially incompressible field. The mean temperature and density are 300K and 1 kg/m^3. Finally, the RMS (root mean square) of density and temperature fluctuations are specified as percentages of the mean density and temperature, respectively. All wavenumbers are distributed on a unit sphere, initially $\|\kappa\| = 1$. The magnitude of initial shear strength (S_0), sound speed and initial length-scale of perturbation determine the initial modal Mach number (3.23).

III.A.1.a. Validation of numerical method

Grid (modal) resolution and time-step studies, along with several other validation investigations of the present RDT scheme, have been presented in Yu et. al [16] and Lavin et al. [10]. The RDT computations recover the analytical Burgers results at the very high Mach number limit when the periodicity of shear is zero. The low Mach number incompressible limit behavior is also confirmed. Inviscid and viscous RDT lead to nearly similar findings – specifically the so-called three-stage behavior is seen for small enough viscosities. Yu et al. [16] show that the present RDT code captures the results of Simone et. al [5] very precisely. Most significantly, Lavin et al. [10] compare RDT anisotropy evolution of steady high-speed homogeneous shear with the DNS data of Sarkar [4] leading to reassuring support of this approach. Detailed convergence studies have been performed in Bertsch et al. [9]

III.B. Individual Effects of Compressibility and Unsteadiness

Before we present our analysis and results, which combine the effects of compressibility and unsteadiness, we summarize what is currently understood about the individual effects. Low-speed or incompressible steady homogeneous shear flow will be used as a base flow to compare the individual effects. Figure III.1 shows the evolution of turbulent kinetic energy for an incompressible uniform shear flow. The evolution at the incompressible limit is deemed unstable because the turbulent kinetic energy continues to grow in magnitude. The unstable growth is caused by the evolution of the turbulent shear stress, $\langle u_1' u_2' \rangle$, which evolves to a large (in magnitude) negative value in the incompressible limit, seen in Figure III.2, leading to large

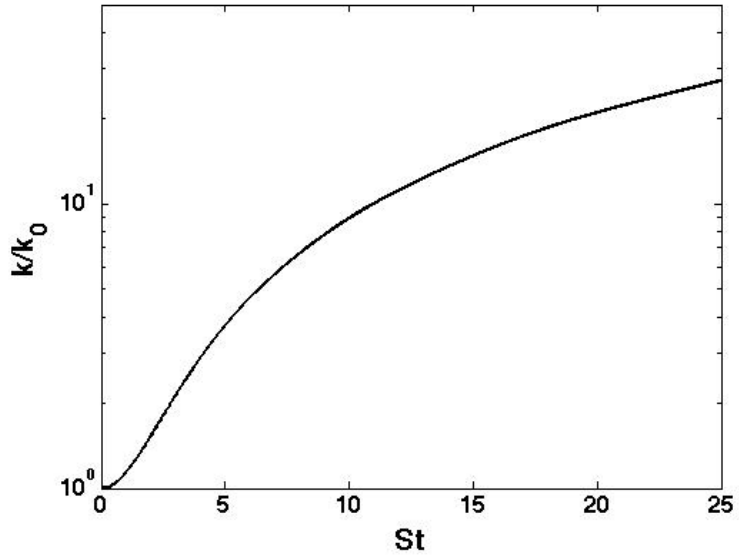

Figure III.1. Evolution of turbulent kinetic energy for incompressible ($M_m = 0.1$) homogeneous shear flow.

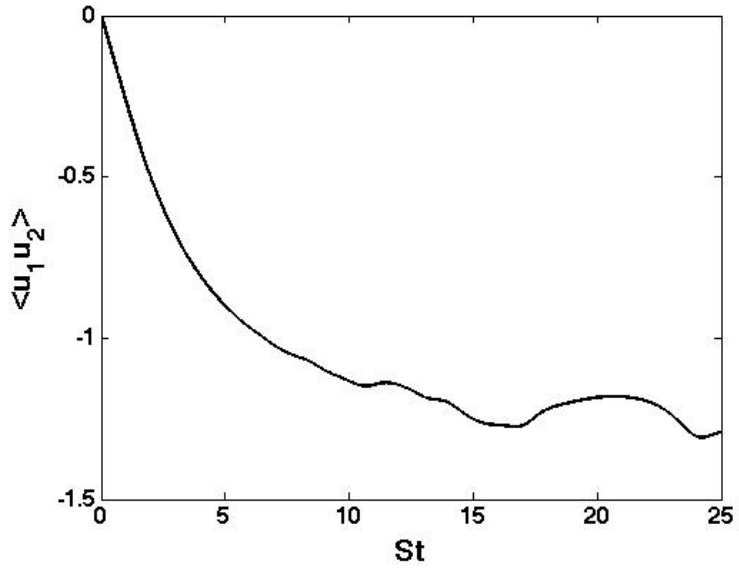

Figure III.2. Evolution of turbulent Reynolds shear stress, $\langle u_1' u_2' \rangle$, for incompressible homogeneous shear flow.

turbulent production. We will use Figures III.1 and III.2 to compare and contrast the evolutions of the turbulent kinetic energy and shear stress for flows subject to compressibility and unsteadiness individually.

In previous studies of compressible steady homogeneous shear flows [9–11, 16], the turbulence field was shown to undergo three stages of evolution due to the changing nature of pressure. This pressure behavior ultimately has a stabilizing influence on the growth of turbulent kinetic energy, as seen in Figure III.3. The three distinct regimes of pressure evolution are summarized. **Regime 1**: When the pressure timescale is significantly large in comparison with shear time scale, pressure exhibits no influence and turbulent kinetic energy evolves along Burgers (or pressure-released) limit. **Regime 2**: The timescales of pressure and shear are of the same order so dilatational waves are created in the flow normal direction and as a result, pressure works to counteract growth in $\langle u_1^{'} u_2^{'} \rangle$, as seen in Figure III.4. **Regime 3**; The small pressure timescale (or the acoustic frequency) can quickly respond to any change in the velocity field due to the shear magnitude and the Reynolds stresses evolve analogous to the incompressible limit. Clearly, pressure action is the stabilizing influence in high-speed/compressible homogeneous shear flows. Based on the aforementioned studies, the physics of compressible homogeneous flows with zero shearing periodicity seem reasonably well understood.

Studies of nonzero periodic [12] and rotational [13] shearing rates have been conducted at the incompressible limit. Both of these studies examine the influence of temporally varying shearing effects. In Yu and Girimaji [12], a DNS study of a periodically varying homogeneous shear flow, examined the effect of an unsteady

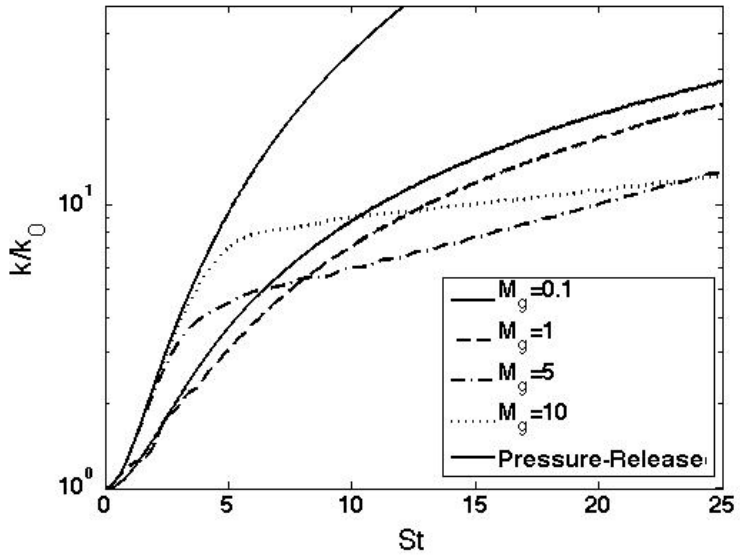

Figure III.3. Evolution of turbulent kinetic energy for various initial modal Mach numbers(M_m). Thin $(-)$ $M_m = 0.1$:Incompressible limit; $(--)$ $M_m = 1$; $(- \cdot -)$ $M_m = 5$; $(\cdots)$ $M_m = 10$; Thick$(-)$ Burger's limit.

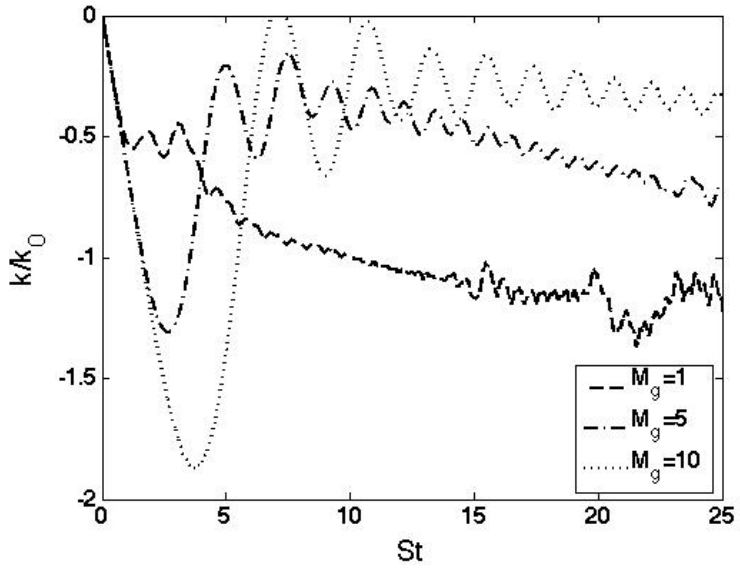

Figure III.4. Evolution of turbulent Reynolds shear stress, $\langle u_1' u_2' \rangle$, for various initial modal Mach numbers(M_m). $(--)$ $M_m = 1$; $(- \cdot -)$ $M_m = 5$; $(\cdots)$ $M_m = 10$.

shearing rate. In Figure III.5, we utilize our RDT approach to simulate the same shearing rate frequencies as Yu and Girimaji at a low Mach number. Our comparison of RDT to DNS results do not show quantitative agreement since the DNS approach encompasses dissipation and turbulent transport terms whereas RDT does not. However, qualitative agreement between Yu & Girimaji's DNS results and our RDT simulation can be seen as the influence of increasing periodic frequency appears to stabilize the growth of turbulent kinetic energy. Upon examination of the turbulent shear stress in Figure III.6, it is clear the rapidly oscillating shear rate is responsible for the reduction in $\langle u_1' u_2' \rangle$. For higher periodic frequencies, the suppression of the turbulent shear stress evolution is stronger. The stabilizing influence of increased unsteadiness is illustrated and evaluated against a constant (or steady) shearing rate.

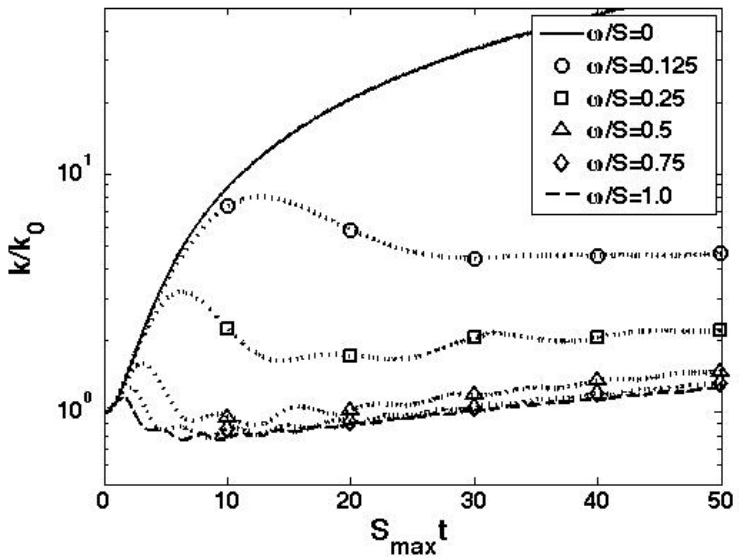

Figure III.5. Evolution of shear magnitude (S) and stress ($\overline{u_1 u_2}$) for steady, incompressible ($M_m = 0.1$) shear.

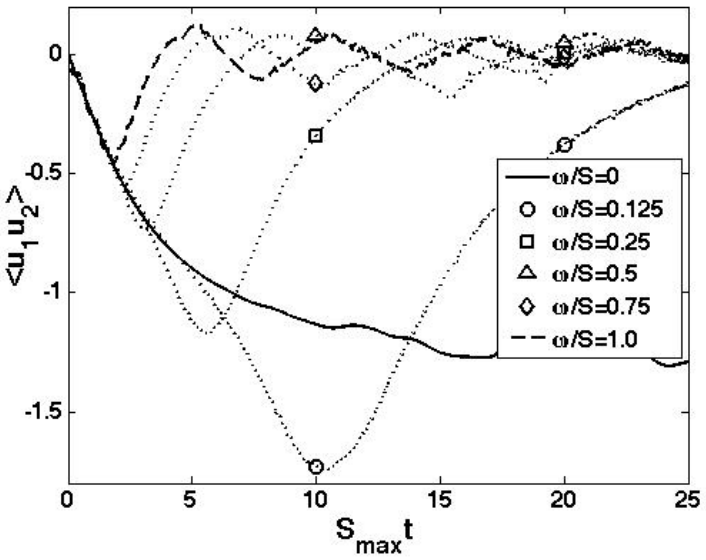

Figure III.6. Evolution of shear magnitude (S) and stress ($\overline{u_1 u_2}$) for incompressible ($M_m = 0.1$) shear flow with an intermediate periodic frequency, $\omega/S_{max} = 1.0$.

Sufficient studies, like the ones summarized, have clearly established the stabilizing influence of unsteadiness on incompressible flow. This paper will provide evidence the stabilizing effect continues well into the compressible regime. In the study that follows, a broad range of forcing frequencies (Table III.1) were chosen to fully examine the influence of periodicity on a high-speed homogeneous shear flow.

Table III.1. Forcing Frequencies

Regime	ω/S
Zero frequency	0.00
	0.10
Low frequency	$0.3\overline{3}$
	0.5
Intermediate frequency	1.00
	2.00
High frequency	3.00
	10.00

III.C. Combined Effects: Analysis of Pressure Fluctuations in Compressible Unsteady Shear Flows

In incompressible flows, the nature of pressure imposes the divergence free condition throughout the field. For compressible flows, the role of pressure is more complex due to its evolution as a thermodynamic variable governed by the wave equation. The nature of pressure at high-speeds is further complicated when the mean flow field becomes time dependent. Following a similar approach to Bertsch et al. [9] and Kumar & Girimaji [11], an analysis of the wave equation for pressure in the compressible unsteady RDT limit will be presented.

Before we begin the pressure equation analysis, we will present the differences in the evolution of the wave-vector in steady and unsteady shear flows. In steady homo-

geneous shear flow, the wavenumber-dependent length scale and the corresponding instantaneous modal Mach number decrease with time as seen in Lavin et al. [10] and Bertsch et al. [9]. The approximate evolution of the modal Mach number for steady homogeneous shear is:

$$M_m(t) \approx \frac{M_m}{St}, \tag{3.24}$$

which clearly decays with time.

For the temporally periodic homogeneous shear case, the instantaneous modal Mach number is distinctly different. From (3.21) and (3.12), we can write:

$$\kappa_1(t) = \kappa_1(0); \quad \kappa_3(t) = \kappa_3(0), \tag{3.25}$$

$$\frac{d\kappa_2}{dt} = -S_0 \cos(\omega t)\kappa_1(t). \tag{3.26}$$

The solution to equation (3.26) can be written as:

$$\kappa_2(t) = \kappa_2(0) - S_0\kappa_1(0)\cos(\omega t). \tag{3.27}$$

Based on this evolution of the wave vector components for the periodic shear case, the instantaneous modal Mach number evolves according to:

$$M_m(t) \approx \frac{M_m}{\sqrt{1 + \frac{S_0^2}{\omega^2}\sin^2(\omega t)}}. \tag{3.28}$$

The normalized modal Mach number can never exceed the limits of:

$$1 \leq \frac{M_m(t)}{M_m(0)} \leq 1/\sqrt{1 + S_0^2/\omega^2}. \tag{3.29}$$

Figure III.7 shows the evolution of the modal Mach number for steady and unsteady shear flows. The steady case decays to incompressible values quickly due to the rapid growth of the wavenumber vectors. As suspected, the modal Mach

numbers of the unsteady cases get trapped in a periodic growth/decay state that never quite reaches low speed values. The significance of the wavenumber and modal Mach number evolutions will be presented later. In this paper we will use the symbol M_m to denote the initial value of modal Mach number in a simulation and the symbol $M_m(t)$ to denote its instantaneous value (3.28) at a later time t.

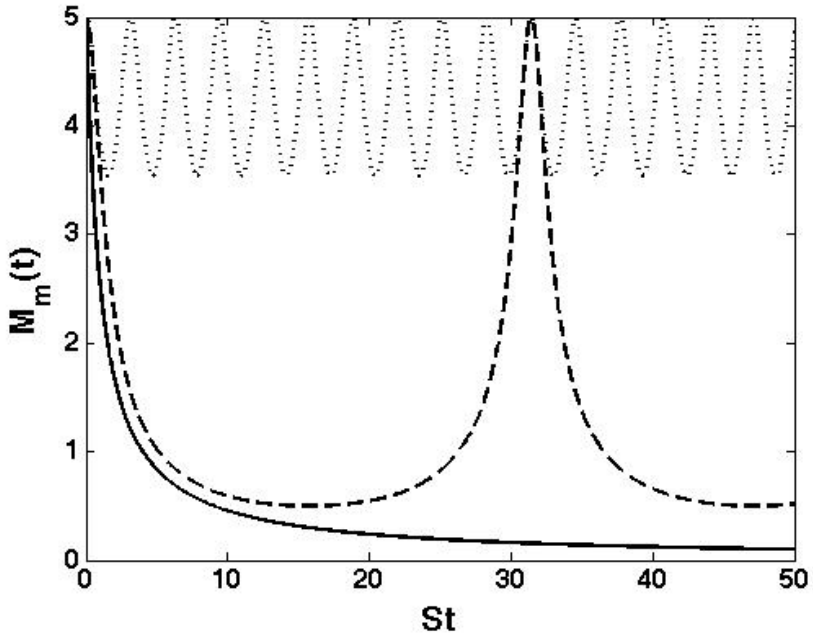

Figure III.7. Evolution of the modal Mach number for zero and nonzero periodic shear. $(-)$,$\omega = 0S : Steady$; $(--)$,$\omega = 0.1S$; $(\cdots)$;$\omega = 1S$.

We begin with the linearized equation of pressure fluctuation in a homogeneous shear flow derived by Livescu et al. [20] for the steady case:

$$\frac{d^3\hat{p}}{dt^3} = -\gamma\overline{\rho}R\overline{T}\left(\kappa^2\frac{d\hat{p}}{dt} - 4\kappa_1\kappa_2 S\hat{p}\right). \tag{3.30}$$

We differentiate equation (3.20) twice to obtain the equation of pressure fluctuations

in an unsteady periodic homogeneous shear flow:

$$\frac{d^3\hat{p}}{dt^3} = -\gamma\overline{\rho}R\overline{T}[\kappa^2\frac{d\hat{p}}{dt} - 4\kappa_1\kappa_2 S_0\cos(\omega t)\hat{p} + 2\frac{\kappa_1\hat{u}_2\overline{\rho}}{i}S_0\omega\sin(\omega t)]. \tag{3.31}$$

Even with the added complexity of unsteadiness, (3.31) is still similar in form to the constant shear pressure equation (3.30).

Despite the linearization, equation (3.31) is still too complicated for any analytical treatment. To draw meaningful insight into the pressure evolution process for periodic shear flows, we subject this equation to further simplifying assumptions. In a periodic homogeneously sheared flow field, the wavenumber vector evolves as:

$$\begin{aligned} \kappa_1(t) &= \kappa_1(0); \\ \kappa_2(t) &= \kappa_2(0) - \frac{\kappa_1(0)S_0}{\omega}\sin(\omega t); \\ \kappa_3(t) &= \kappa_3(0). \end{aligned} \tag{3.32}$$

It is evident that the pressure fluctuation behavior will depend on the magnitude of the ratio of the initial shear rate to periodic frequency S_0/ω.

III.C.1. High frequency regime

In the high frequency limit, $\frac{S_0}{\omega} < 1$, equation (3.32) reveals that the wave-number vector remains nearly constant in time. The second term in the evolution expression for κ_2, which is solely responsible for the growth of the wave-number vector in steady shear flows, is restricted by the periodic shear rate. At high frequencies this term is small and oscillates rapidly. As a result, the magnitude of κ remains close to it's initial value. The production and pressure-strain terms of the Reynolds stress

evolutions do not have adequate time to evolve through the three stages found in steady high-speed homogeneous shear flows. The turbulent quantities of the high frequency cases will oscillate about their initial values, similar to the high frequency cases in the incompressible study of Girimaji et al. [13]

III.C.2. Low frequency regime

In the low frequency limit, $\frac{S_0}{\omega} > 1$, we can adapt the analysis outlined in Bertsch et al. [9]. It is clear that κ_2 is the dominant term in equation (3.32) which permits the simplification:

$$|\kappa(t)| \approx |\kappa_2(t)| \approx |\kappa_1| \frac{S_0}{\omega} \sin(\omega t). \tag{3.33}$$

With this approximation, equation (3.31) can be written as:

$$\begin{aligned} \frac{d^3\hat{p}}{dt^3} \approx -c_0^4 \quad [\quad & \sin^2(\omega t)\frac{d\hat{p}}{dt} - 4\omega \cos(\omega t)\sin(\omega t)\hat{p} \\ + \quad & 2\frac{\hat{u}_2 S_0 \kappa_1(0)\omega\overline{\rho}}{i}\sin(\omega t)], \end{aligned} \tag{3.34}$$

where $c_0 = \sqrt{(a_0 k_1(0) S_0/\omega)}$. This quantity can be recognized as the geometric mean of the imposed mean strain and initial acoustic frequency. Following the analysis in Bertsch et al., equation (3.34) can be rewritten as:

$$\frac{d^3\hat{p}}{dt^3} + q\frac{d\hat{p}}{dt} + r\hat{p} + m \approx 0, \tag{3.35}$$

where:

$$\begin{aligned} q &= c_0^4 \sin^2(\omega t) \\ r &= -4c_0^4 \omega \sin(\omega t)\cos(\omega t) \\ m &= \frac{2\hat{u}_2 c_0^4 \omega^3}{\kappa_1(0) S_0}\sin(\omega t). \end{aligned} \tag{3.36}$$

Equation (3.35) is a third order inhomogeneous ordinary differential equation with time-dependent coefficients. For the purposes of this study, we will focus on finding the general solution of the associated homogeneous equation:

$$\frac{d^3\hat{p}}{dt^3} + q\frac{d\hat{p}}{dt} + r\hat{p} \approx 0. \tag{3.37}$$

Deriving an analytical general solution of the homogeneous part of equation (3.37) is still not straightforward. We assume the coefficients (q and r) of equation (3.37) are locally constant in order to attain qualitative analysis into the interaction between acoustic and shear timescales. This method allows us to predict the general solution of equation (3.37) as:

$$\hat{p}(t) \sim \hat{p}_0 e^{yt}. \tag{3.38}$$

Substituting (3.38) into (3.37), we obtain a cubic equation for the unknown exponent y:

$$y^3 + qy + r = 0. \tag{3.39}$$

Continuing with the analysis outlined in Bertsch et al. [9], we define two intermediate variables s_1 and s_2 for a periodic shear case as:

$$\begin{aligned} s_1 &= [-2c_0^4\omega\sin(\omega t)\cos(\omega t) \\ &+ (\frac{c_0^{12}\sin^6(\omega t)}{27} + 4c_0^8\omega^2\sin^2(\omega t)\cos^2(\omega t))^{\frac{1}{2}}]^{\frac{1}{3}}, \\ s_2 &= [-2c_0^4\omega\sin(\omega t)\cos(\omega t) \\ &- (\frac{c_0^{12}\sin^6(\omega t)}{27} + 4c_0^8\omega^2\sin^2(\omega t)\cos^2(\omega t))^{\frac{1}{2}}]^{\frac{1}{3}}. \end{aligned} \tag{3.40}$$

The three possible roots for the exponent equation (3.39) are written as:

$$\begin{aligned} y_1 &= (s_1 + s_2), \\ y_2 &= -\frac{1}{2}(s_1 + s_2) + \frac{i\sqrt{3}}{2}(s_1 - s_2), \\ y_3 &= -\frac{1}{2}(s_1 + s_2) - \frac{i\sqrt{3}}{2}(s_1 - s_2). \end{aligned} \tag{3.41}$$

The real parts of the equation (3.41) represent the growth rate of pressure fluctuations and the imaginary parts represent the frequency of oscillations. Equations (3.40) and (3.41) demonstrate that although forced periodic unsteadiness adds complexity to the intermediate variable expressions, the overall analytical estimate remains virtually identical to the steady homogeneous shear case found in Bertsch et al. [9].

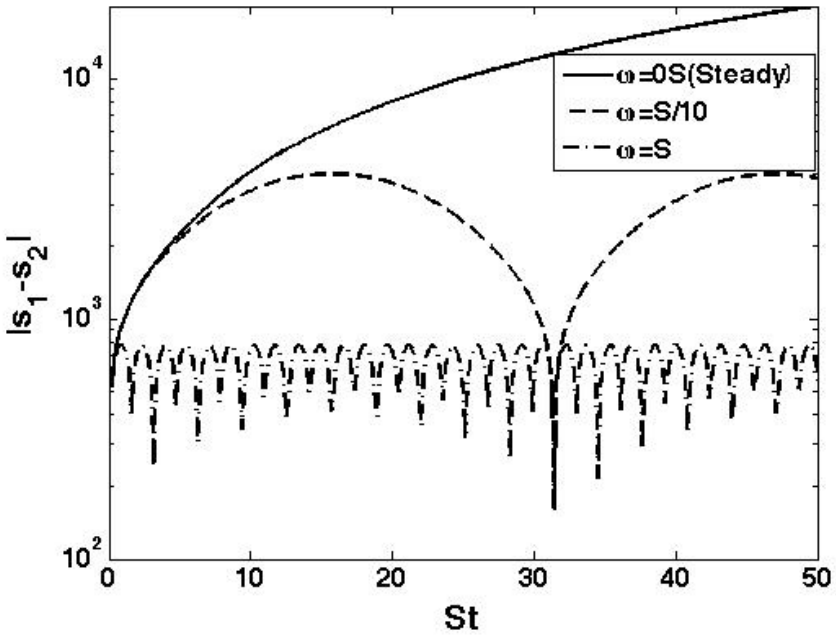

Figure III.8. Evolution of $|s_1 - s_2|$ for compressible initial modal Mach numbers($M_m = 5$) and various frequencies(ω).

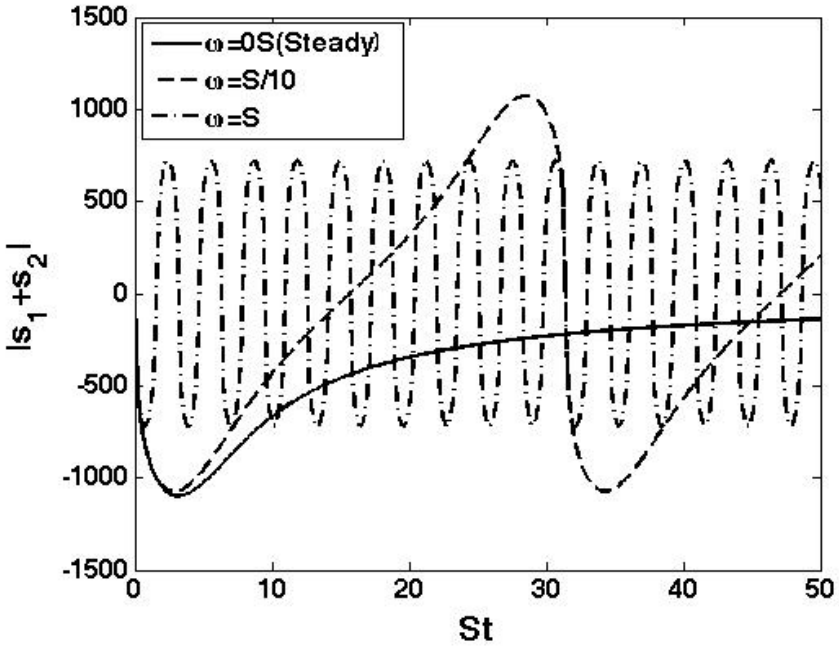

Figure III.9. Evolution of $|s_1 + s_2|$ for compressible initial modal Mach numbers($M_m = 5$) and various frequencies(ω).

For the constant shear case, Bertsch et al. [9] have shown the frequency of pressure fluctuations monotonically increases with time. For the periodic shear case, Figure III.8 shows that the frequency of oscillations (imaginary part of (3.41)) no longer grows monotonically but instead departs from of the evolutionary path for the constant shear case and exhibits a cyclic behavior dependent on the frequency of periodicity, ω. The relative magnitude of the acoustic frequencies with respect to the time scale of mean fluid motion (S) limits the range of values in the periodic shear cases. Figure III.9 also demonstrates the growth rates of the periodic shear cases behave in a different manner than the steady case. Whereas the real part of the exponential roots in the constant shear case appears to have a large growth rate

initially that slowly tends to an asymptotic value, the real parts of the unsteady cases exhibit oscillatory behavior about a mean value of zero.

III.C.2.a. Early time behavior

Similar to the analysis in Bertsch et al. [9], we consider the limiting behavior of s_1 and s_2 at very early times:

$$\begin{aligned}\lim_{t\to 0}|s_1 - s_2| &= \lim_{t\to 0}|[(-2c_0^4\omega\sin(\omega t)\cos(\omega t) \\ &+ (\frac{c_0^{12}\sin^6(\omega t)}{27} + 4c_0^8\omega^2\sin^2(\omega t)\cos^2(\omega t))^{\frac{1}{2}}]^{\frac{1}{3}} \\ &- [-2c_0^4\omega\sin(\omega t)\cos(\omega t) \\ &- (\frac{c_0^{12}\sin^6(\omega t)}{27} + 4c_0^8\omega^2\sin^2(\omega t)\cos^2(\omega t))^{\frac{1}{2}}]^{\frac{1}{3}}|.\end{aligned} \tag{3.42}$$

In this limit, we utilize the small angle approximation ($\sin(\omega t) \approx \omega t$ and $\cos(\omega t) \approx 1 - \frac{(\omega t)^2}{2}$). Neglecting terms with higher orders of t reduces the approximation to:

$$|s_1 - s_2| \approx \left(4c_0^4\omega^2 t\right)^{1/3}, \tag{3.43}$$

which is very similar to the expression for the early time behavior of this quantity in the constant shear case. Thus the pressure field frequency evolves in time as:

$$\frac{1}{|s_1 - s_2|} \approx \frac{1}{4^{1/3}c_0^{4/3}\omega^{2/3}t^{1/3}}. \tag{3.44}$$

For times that are small compared to the pressure frequency:

$$t < \frac{1}{4^{1/3}c_0^{4/3}\omega^{2/3}t^{1/3}}, \tag{3.45}$$

the pressure field can be taken to be nearly stationary. During this time, the pressure field will not exert any influence on the velocity field. This is called the pressure-release turbulence limit wherein the velocity field evolves solely driven by inertial

effects. As pointed out in Cambon [21] and Bertsch et al. [9], this situation is akin to Burgers turbulence. This time period is what Bertsch et al. refer to as the first regime of kinetic energy evolution. Using the definition $c_0 = \sqrt{(a_0 k_1(0) S_0/\omega)}$, (3.45) can be expressed as:

$$t < \frac{1}{4^{1/3}\left(\frac{a_0 k_1(0) S_0}{\omega}\right)^{2/3} \omega^{2/3} t^{1/3}}. \tag{3.46}$$

Further simplification and using the definition of modal Mach number (3.23), the duration of the first regime can be expressed as:

$$\frac{S_0 t}{\sqrt{M_m(t)}} < \frac{1}{4^{1/4}} \approx \frac{1}{\sqrt{2}}. \tag{3.47}$$

Referring to Figure III.5, $St \approx \sqrt{M_m/2}$ is the time at which the kinetic energy evolution transitions from stage 1 to stage 2. Therefore, the analysis of the pressure equation suggests the presence of a regime in periodically sheared turbulence wherein pressure evolution is too slow to influence the velocity field (and thus the kinetic energy). In this regime the velocity field grows solely by the effects of inertia. This hypothesis will be investigated in the next section by performing RDT computations.

III.C.2.b. Beyond early time behavior

Next we consider the acoustic frequencies in equation (3.39) at later times. Since all the terms in equation (3.40) are periodic in time, it stands to reason that beyond

the early time limit, the frequency of acoustic oscillations can be written as:

$$\begin{aligned}\lim_{t\to\infty}|s_1-s_2| &= \lim_{t\to\infty}|[(-2c_0^4\omega\sin(\omega t)\cos(\omega t) \\ &+ (\frac{c_0^{12}\sin^6(\omega t)}{27}+4c_0^8\omega^2\sin^2(\omega t)\cos^2(\omega t))^{\frac{1}{2}}]^{\frac{1}{3}} \\ &- [-2c_0^4\omega\sin(\omega t)\cos(\omega t) \\ &- (\frac{c_0^{12}\sin^6(\omega t)}{27}+4c_0^8\omega^2\sin^2(\omega t)\cos^2(\omega t))^{\frac{1}{2}}]^{\frac{1}{3}}|.\end{aligned} \tag{3.48}$$

The amplitude of the pressure field frequency is then bounded by:

$$\lim_{t\to\infty}|s_1-s_2| \leq 2|(-2c_0^4\omega)^{\frac{1}{3}}|+2|(\frac{c_0^{12}}{27}+4c_0^8\omega^2)^{\frac{1}{6}}| \tag{3.49}$$

If we plug in our expression for c_0, utilize equation (3.23), and note that the frequency ω is a scalar multiple of the shear magnitude, S_0, we can find the limits in terms of the periodic frequency and initial Mach number:

$$\begin{aligned}|(2c_0^4\omega)^{\frac{1}{3}}| &\approx 2\left(\frac{S_0}{\omega}\right)^{\frac{2}{3}}\left(\frac{1}{M_{g,0}}\right)^{\frac{2}{3}}S_0 \\ |\left(\frac{c_0^{12}}{27}+4c_0^8\omega^2\right)^{\frac{1}{6}}| &\approx \left(\frac{S_0}{\omega}\right)\left(\frac{1}{M_{g,0}}\right)S_0 \\ &+ 4\left(\frac{S_0}{\omega}\right)^{\frac{2}{3}}\left(\frac{1}{M_{g,0}}\right)^{\frac{2}{3}}S_0\end{aligned} \tag{3.50}$$

In the hypersonic, low frequency case, we further have:

$$\frac{S_0}{\omega}\geq 1 \quad and \quad M_{g,0}>1. \tag{3.51}$$

Therefore,

$$\begin{aligned}\frac{(2c_0^4\omega)^{\frac{1}{3}}}{S_0} &\leq O(1) \\ \frac{1}{S_0}\left(\frac{c_0^{12}}{27}+4c_0^8\omega^2\right)^{\frac{1}{6}} &\leq O(1)\end{aligned} \tag{3.52}$$

Finally we obtain:

$$\lim_{t\to\infty} \frac{|s_1 - s_2|}{S_0} \approx O(1). \tag{3.53}$$

The ratio of pressure to shear frequency is of order unity or smaller. This corresponds to Regime 2 in Bertsch et al. [9] In the periodic shear case transition to Regime 3 does not occur. The pressure evolution is frozen in what Bertsch et al. refer to as Regime 2 where the flow field and pressure timescales are of the same magnitude.

In summary, the analysis of the pressure equation leads to three vital inferences:

1. The early flow field evolution in the periodic shear flow is similar to the steady shear counterpart.

2. At later times, the pressure and flow field exhibit Regime 2 behavior.

3. Due to the boundaries of the pressure-field frequency, Regime 3 (in Bertsch et al. [9]) is inaccessible to periodically forced turbulence.

We will now perform RDT computations to verify the above inferences.

III.D. RDT Velocity Field Behavior

In this section, we discuss our observations from the results of the periodic shear RDT simulations. We focus on three distinct flow field quantities: turbulent kinetic energy, anisotropy and the equi-partition function. We also examine the evolution of shear versus stress for compressible periodic shear. Each of these quantities are reasonably well understood in steady compressible homogeneous shear flows, which make them ideal for comparison with our periodic shear cases.

III.D.1. Turbulent kinetic energy

Since inviscid RDT entails assumptions and simplifications that result in a linear analysis approach, the Reynolds stress evolution equation reduces to:

$$\frac{d\overline{u_i{}'u_j{}'}}{dt} = P_{ij} - \Pi_{ij}. \tag{3.54}$$

In the linear regime, the Reynolds stresses are only influenced by production, P_{ij}, of velocity fluctuations and the rapid pressure strain correlation, Π_{ij}. In the compressible regime, the production can be quite large since it is directly dependent on the shearing rate:

$$P_{ij} = -\overline{u_i{}'u_k{}'}\frac{\partial\overline{U_j}}{\partial x_k} - \overline{u_j{}'u_k{}'}\frac{\partial\overline{U_i}}{\partial x_k}. \tag{3.55}$$

To counteract this rapid growth, the pressure-strain correlation must redistribute the additional energy along the other coordinates via pressure:

$$\Pi_{ij} = \overline{p'(\frac{\partial u_i{}'}{\partial x_j} + \frac{\partial u_j{}'}{\partial x_i})}. \tag{3.56}$$

Utilizing equations (3.12, 3.55, and 3.56), it is clear the evolution of kinetic energy is governed by:

$$\frac{dk}{dt} = \frac{d\overline{u_i'u_i'}}{dt} = P_{11} + \Pi_{ii} = -2S_0\cos(\omega t)\overline{u_1'u_2'} + \Pi_{ii}. \tag{3.57}$$

It is evident that the periodic shear rate influences the growth rate of kinetic energy. Figure III.10 presents the effect of periodic frequency on three modal Mach numbers, $M_m = 1, 5, 10$. Since the shear periodicity is dependent on the initial Mach number, all three figures look qualitatively similar. In these figures, all the periodic shear cases depart from the constant shear evolutionary path in a similar manner to the different modal Mach number cases peeling off of the Burger's limit evolution path in

Figure III.3. Bertsch et al. [9] explain that this departure marks the transition into the second stage of pressure evolution where $M_m(t) \approx \sqrt{M_m(0)}$. Based on equation (3.28), the higher the periodic frequency, ω, the earlier the transition into the second regime occurs. As seen in the analysis section (III.C), the periodic shear cases get trapped in the second regime due to the oscillations in the velocity field. The rapidly changing shear rate prevents the modal Mach number from achieving the incompressible limit and therefore prevents the pressure field from reaching the third evolution regime. Figure III.10 shows intermediate and high periodic shear frequencies exhibiting kinetic energy growth that is less than 20% of the constant or steady shear case. For really large frequencies ($\omega > 3S_0$), the energy has insufficient time to evolve and remains nearly constant. Based on these observations, forced periodic shearing appears to be a stabilizing influence on laminar transition to turbulence.

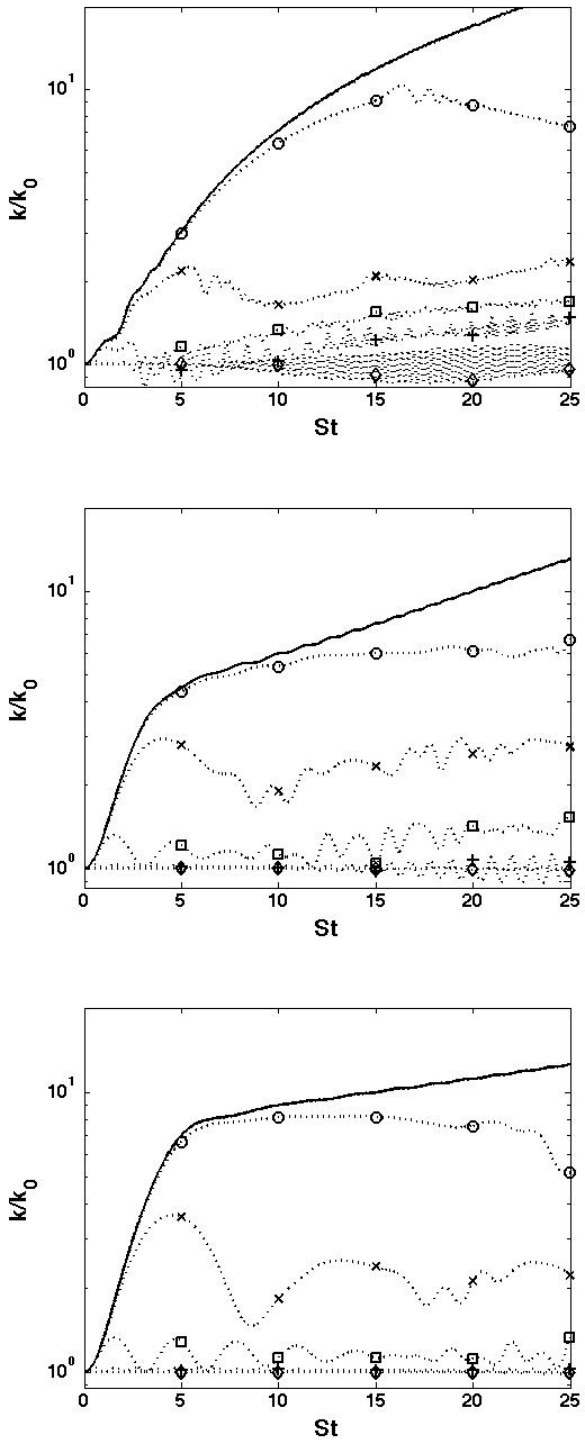

Figure III.10. Evolution of turbulent kinetic energy for varying frequencies for initial modal Mach numbers a)$M_m = 1$, b)$M_m = 5$, and c)$M_m = 10$. Legend: $(-)$ $\omega = 0S$: *Steady*; $(\circ)$ $\omega = 0.1S$; (X) $\omega = 0.33S$; $(\square)$ $\omega = 1S$; $(+)$ $\omega = 3S$; $(\diamond)$ $\omega = 10S$.

III.D.2. Anisotropy

Other flow field quantities of interest are the components of the Reynolds stress anisotropy tensor, defined as:

$$b_{ij} = \frac{\overline{u_i' u_j'}}{2k} - \frac{1}{3}\delta_i j. \tag{3.58}$$

The components of the anisotropy tensor measure the amount of energy contained along each flow direction.

We analyze these components in a similar manner to Girimaji et al. [13] by examining the low frequency and high frequency cases separately. Figure III.11 shows the low frequency (a) and high frequency (b) cases of b_{11}. For the incompressible case, Girimaji et al. observed that the steady case of b_{11} asymptotes to the maximum possible value, given adequate time to evolve. This indicates all the turbulent kinetic energy ends up in b_{11}. They observed that low frequency forcing caused this term to tend to the lowest possible value, suggesting that all the kinetic energy was contained along the other flow directions. For our compressible study, the steady or zero forcing case b_{11} value appears to asymptote around a value of 0.45, indicating that some of the kinetic energy is aligned along one or both of the other flow field directions. In Figure III.11a, the low frequency periodicity cases tend to near zero or negative values similar to the incompressible case. This suggests low frequency forcing causes the kinetic energy to redistribute along the other directions.

For high frequency forcing, Figure III.11b shows b_{11} transitioning from a negative valued asymptote to a near zero value. For higher frequencies of periodic shearing, the value of b_{11} does not have adequate to evolve as the shear rate is oscillating so rapidly and as a result, remains close to its initial value. The near zero value for the

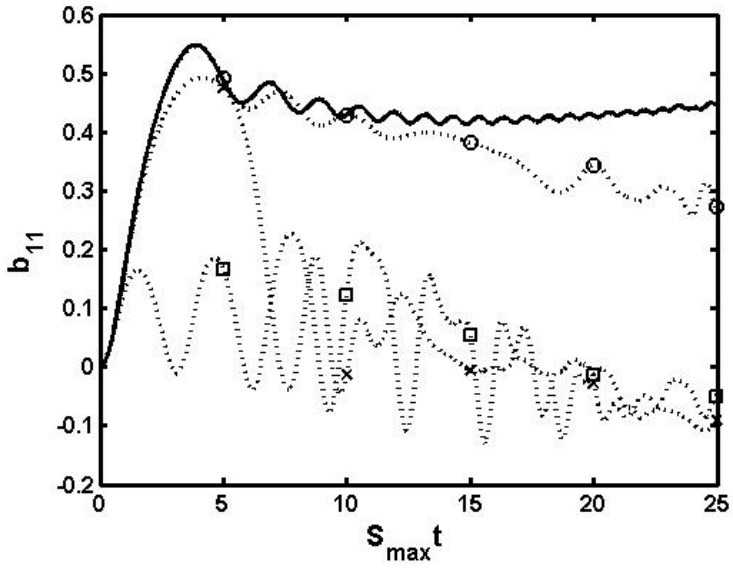

(a)

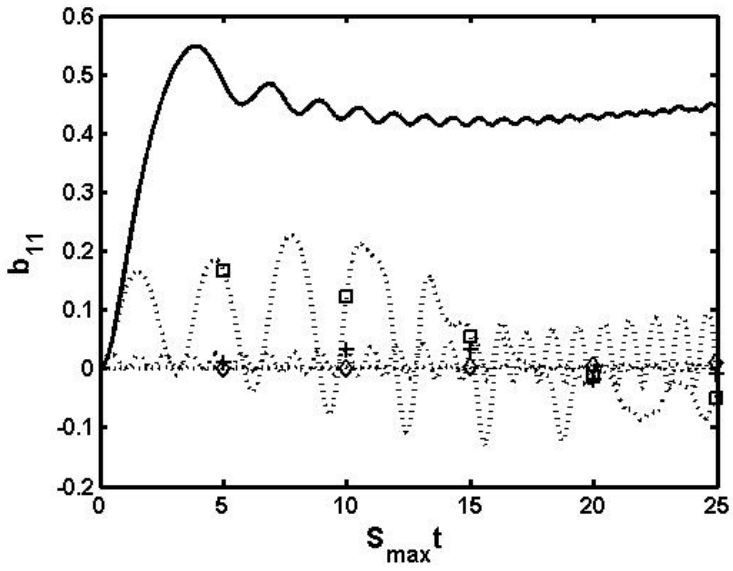

(b)

Figure III.11. Evolution of b_{11} for initial modal Mach numbers($M_m = 5$) for a) a range of low frequency ω and b) a range of high frequency ω. Legend: $(-)$ $\omega = 0S$: *Steady*; $(\circ)$ $\omega = 0.1S$; (X) $\omega = 0.33S$; $(\square)$ $\omega = 1S$; $(+)$ $\omega = 3S$; $(\diamond)$ $\omega = 10S$.

highest frequencies suggest that either the kinetic energy is distributed among each of the $\langle u_i' u_i' \rangle$ components equally or the shear rate is oscillating so quickly, the flow field does not have adequate time to evolve beyond the initial conditions. To verify this theory, an examination of the other components is required. We also note the decreased amplitude of oscillations for higher frequencies which qualitatively agrees with the incompressible study in Girimaji et al. [13].

Figure III.12 presents the low frequency (a) and high frequency (b) evolutions of b_{12}. Yu and Girimaji [12] refer to this component as the shear anisotropy because it plays a crucial role in the production of turbulent kinetic energy. In Figure III.12, the constant shear case of b_{12} (and production by association) experiences a sudden increase in the initial stage. After reaching a peak value, this component eventually settles at a small positive value due to the action of pressure, which is consistent with Bertsch et. al [9]. For all periodic shear cases, a departure or transition from the zero frequency path occurs at times directly dependent on the magnitude of shear frequency. This agrees with the kinetic energy evolution in Figure III.10 as well as the pressure equation analysis in the previous section. The low frequency (Figure III.12a) cases show the departure off the steady path is followed by large amplitude oscillations that appear to develop multiple timescales of evolution. This complex evolution could be explained by the development of a phase lag between the shear anisotropy b_{12} and the instantaneous shear rate, S, introduced by Yu and Girimaji. Showing consistency with b_{11}, the low frequency cases at late times approach a small negative value. The high frequency cases, seen in figure III.12b, see a reduction in the oscillation amplitudes for higher frequencies. At late times, the highest frequency

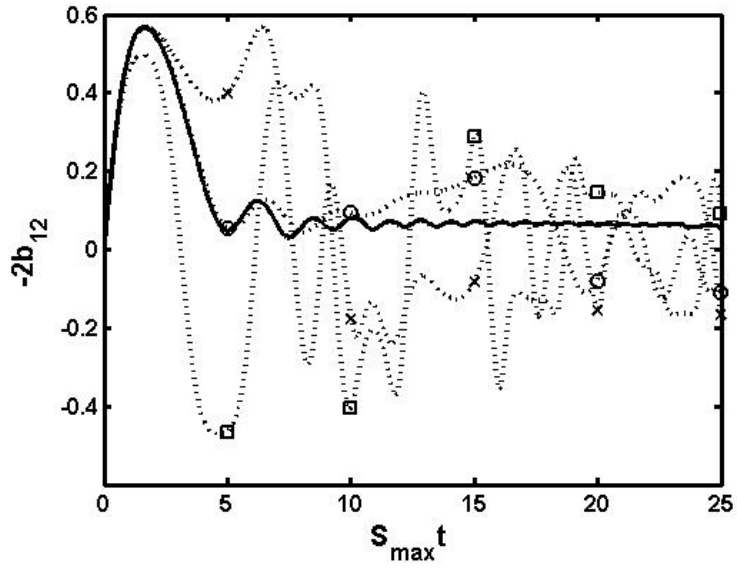

(a)

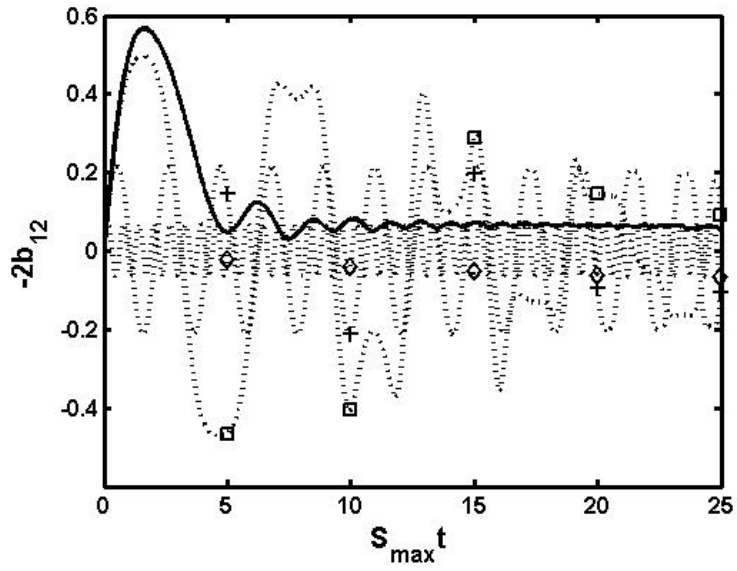

(b)

Figure III.12. Evolution of b_{12} for initial modal Mach numbers($M_m = 5$) for a) a range of low frequency ω and b) a range of high frequency ω. Legend: $(-)$ $\omega = 0S$: *Steady*; $(\circ)$ $\omega = 0.1S$; (X) $\omega = 0.33S$; $(\square)$ $\omega = 1S$; $(+)$ $\omega = 3S$; $(\diamond)$ $\omega = 10S$.

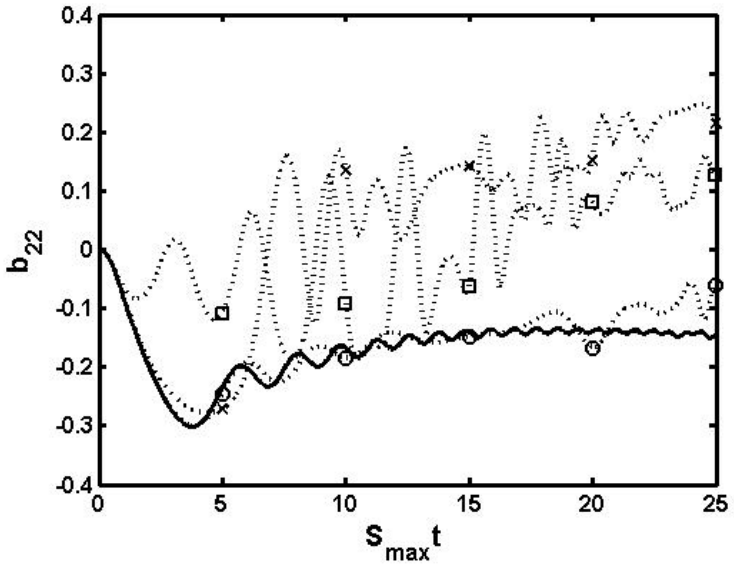

(a)

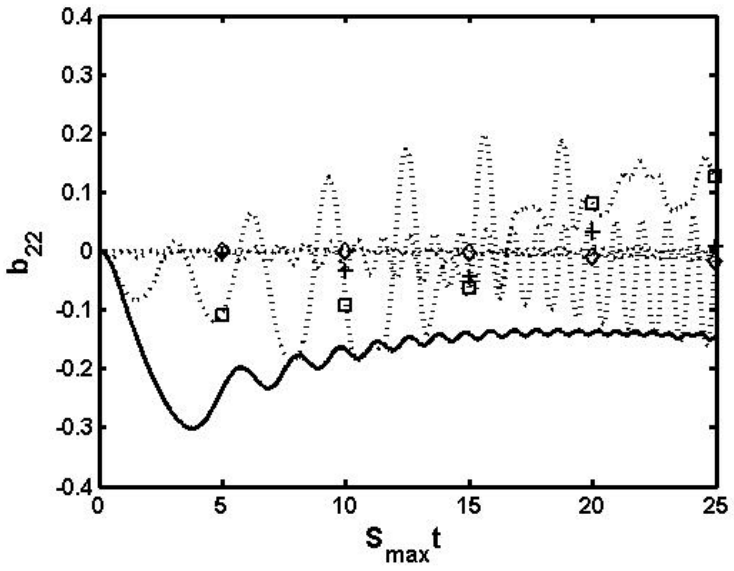

(b)

Figure III.13. Evolution of b_{22} for initial modal Mach numbers($M_m = 5$) for a) a range of low frequency ω and b) a range of high frequency ω. Legend: $(-)$ $\omega = 0S : Steady$; $(\circ)$ $\omega = 0.1S$; (X) $\omega = 0.33S$; $(\square)$ $\omega = 1S$; $(+)$ $\omega = 3S$; $(\diamond)$ $\omega = 10S$.

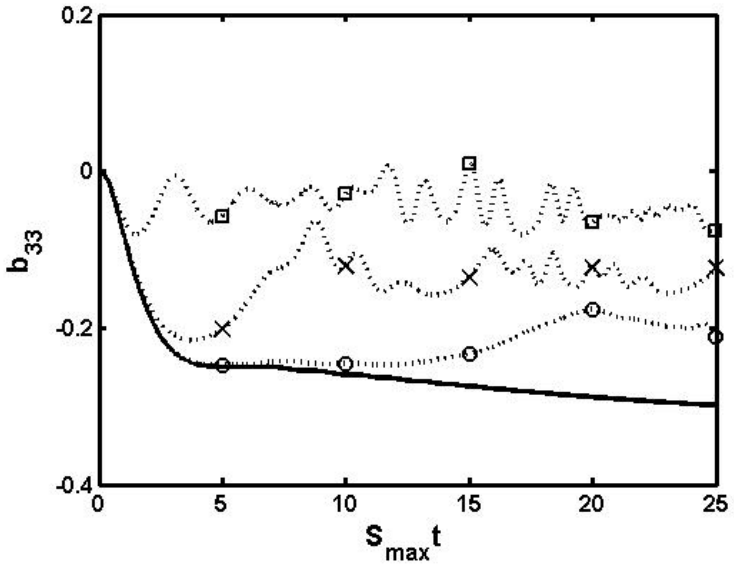

(a)

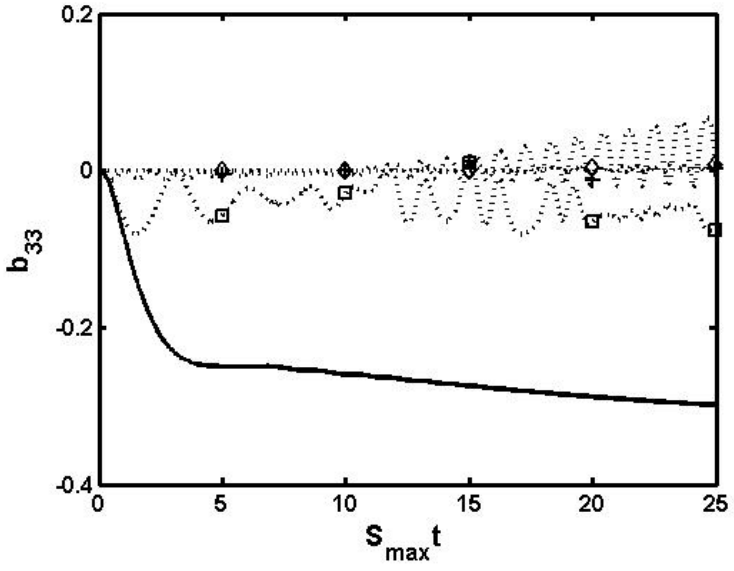

(b)

Figure III.14. Evolution of b_{33} for initial modal Mach numbers($M_m = 5$) for a) a range of low frequency ω and b) a range of high frequency ω. Legend: $(-)$ $\omega = 0S$: *Steady*; $(\circ)$ $\omega = 0.1S$; (X) $\omega = 0.33S$; $(\square)$ $\omega = 1S$; $(+)$ $\omega = 3S$; $(\diamond)$ $\omega = 10S$.

cases rapidly oscillate about a mean value of zero.

The evolutions of b_{22} and b_{33} for constant and periodic shear cases are presented in Figures III.13 and III.14. The steady or zero frequency case for b_{22} qualitatively agrees with the evolution of b_{22} found in Kumar and Girimaji [11]. Our steady simulation does not asymptote near a value of $-1/3$ like the case found in Kumar and Girimaji, but their study was a DNS simulation and we utilized several linearization assumptions. Low periodic frequency cases, seen in Figure III.13a and III.14a, display transitions off the steady case that tend to more positive values of b_{22} and b_{33}. The intermediate frequency, $\omega = 1S$, starts to exhibit a decrease in oscillatory amplitudes. Figures III.13b and III.14b show the high frequency cases tend toward zero beyond the intermediate frequency. Again, we see oscillations of the highest frequency cases exhibit the smallest amplitudes. Like the b_{11} evolution, this trend towards zero suggests that either the kinetic energy is contained in all three components equally or none of the anisotropy components evolve beyond their initial values.

III.D.3. Shear versus stress

In Figure III.15, the instantaneous shear magnitude and Reynolds shear stress are presented for the compressible constant shear case. Once again, the turbulent shear stress tends to a lower asymptotic value than the incompressible case due to the action of pressure. With the addition of periodicity to the compressible uniform shear flow, the behavior of the Reynolds stress is dramatically altered in Figure III.16. A clear phase shift between the two evolutions exists which agrees with the phase lag found in the low-speed case of Yu & Girimaji [12]. What is most intriguing about

Figure III.16 is how the evolution of the shear stress, $\langle u_1' u_2' \rangle$, appears to develop multiple frequencies or periods at later times. This behavior has not been seen in incompressible cases suggesting this could be an effect of compressibility.

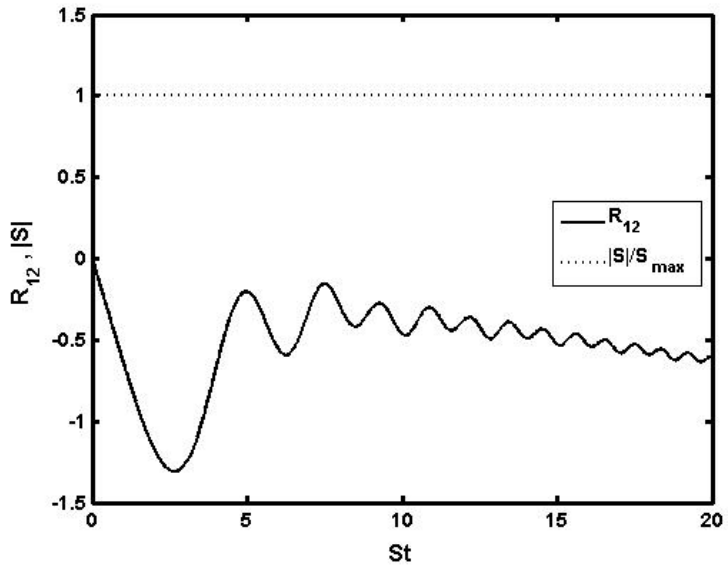

Figure III.15. Evolution of shear magnitude (S) and stress ($\overline{u_1 u_2}$) for steady, compressible ($M_m = 5$) shear.

Plotting the two flow quantities against each other allows for further examination of the evolutionary differences between the shear rate and the shear stress. In a steady homogeneous shear case plotting shear magnitude versus stress results in a simple horizontal line since the shearing rate remains constant. For an ideal unsteady periodic case where both quantities maintain the same period of evolution, the result would produce an elliptical plot. In Figure III.17, the shear rate versus Reynolds stress for an intermediate periodic frequency is presented at earlier times (a) $St =$

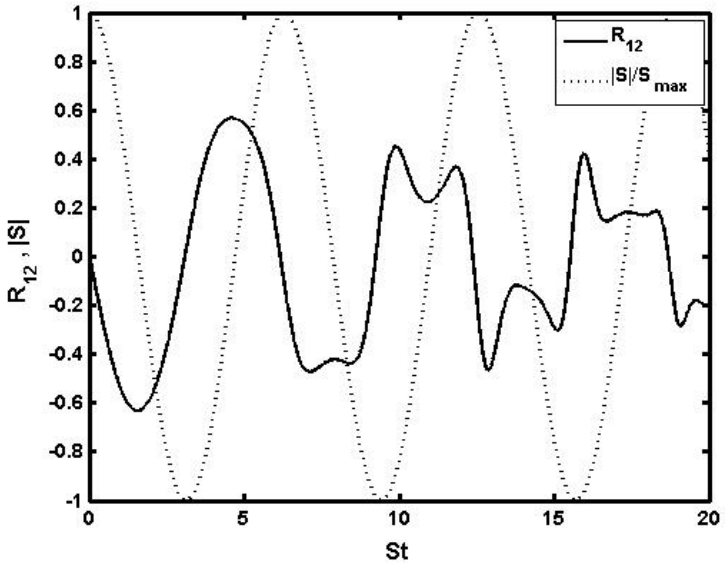

Figure III.16. Evolution of shear magnitude (S) and stress ($\overline{u_1 u_2}$) for compressible ($M_m = 5$) shear flow with an intermediate periodic frequency, $\omega/S_{max} = 1.0$.

$0 - 10$, and later times (b) $St = 10 - 20$. At early times, an elliptical behavior of shear versus stress is observed implying that the phase lag between them is nearly constant during the first cycle ($St \approx 2\pi$) and both quantities evolve as the stress is evolving at the same frequency as the forced shear rate. However, Figure III.17b shows the turbulent Reynolds stress develops multiple evolutionary frequencies at later times (also seen in Figure III.16) producing a departure from the ideal elliptical path. Plotting the evolutions in this manner shows that although the shear rate maintains its periodicity, the period of the Reynolds stress changes with time. Figure III.17 provides concrete evidence that both phase lag and period differences emerge between the shear magnitude and the shear Reynolds stress when subject to high-speed periodic mean shear.

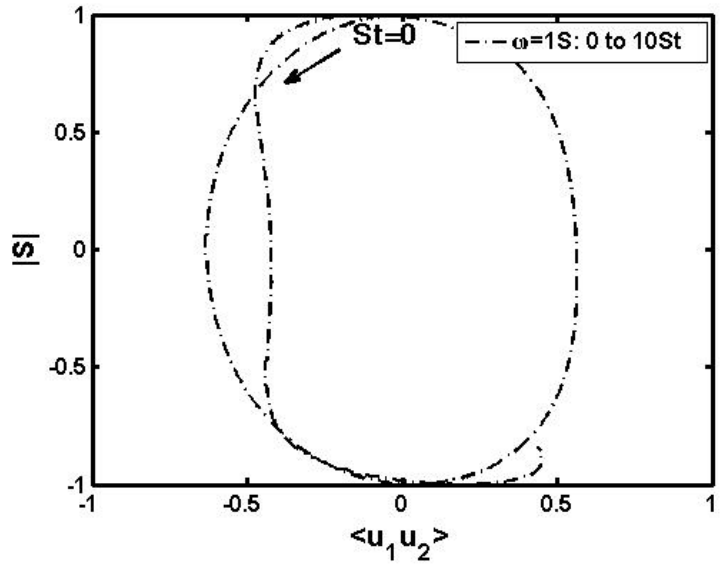

(a)

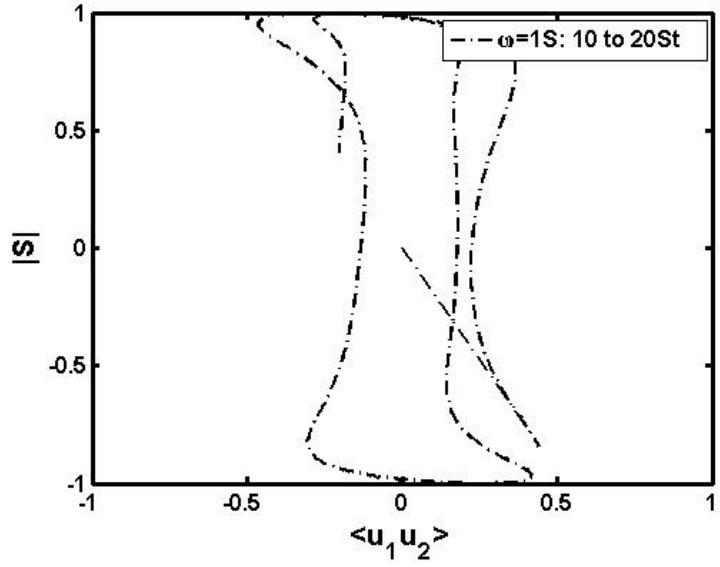

(b)

Figure III.17. Shear magnitude evolution versus stress evolution ($\overline{u_1 u_2}$) for compressible ($M_m = 5$) shear flow with an intermediate periodic frequency, $\omega/S_{max} = 1.0$ for (a)$St = 0 - 10$ and (b)$St = 10 - 20$.

III.D.4. Equipartition between pressure and dilatational kinetic energy

To complete this study we look at the relationship between pressure and dilatational kinetic energy in the compressible periodic shear case to determine how it compares with the constant shear case. We begin with the linearized equations of pressure and spanwise velocity fluctuations:

$$\frac{\partial p^{'}}{\partial t} + \overline{U_k}\frac{\partial p^{'}}{\partial x_k} = -\gamma\overline{p}\frac{\partial u_i}{\partial x_i} \tag{3.59}$$

and

$$\frac{\partial u_2^{'}}{\partial t} + \overline{U_k}\frac{\partial u_2^{'}}{\partial x_k} = -\gamma\frac{1}{\overline{\rho}}\frac{\partial p^{'}}{\partial x_2} \tag{3.60}$$

The second order moments of these two quantities, the derivations for which are detailed in Lavin [18] and Bertsch [22], are governed by the following equations:

$$\frac{d\overline{p^{'}p^{'}}}{dt} = -2\gamma\overline{p}\overline{p^{'}\frac{\partial u_i^{'}}{\partial x_i}} \tag{3.61}$$

and

$$\frac{d\overline{u_2^{'}u_2^{'}}}{dt} = -2\gamma\frac{1}{\overline{\rho}}\overline{p^{'}\frac{\partial u_2^{'}}{\partial x_2}}. \tag{3.62}$$

Using equation (3.62) to replace the left hand side of equation (3.61), the two equations can be combined as:

$$\frac{d\overline{u_2^{'}u_2^{'}}}{dt} = \frac{1}{\overline{\rho}}\left(-\frac{1}{\gamma\overline{p}}\frac{d\overline{p^{'}p^{'}}}{dt} - 2\overline{p^{'}\frac{\partial u_1}{\partial x_1}} - 2\overline{p^{'}\frac{\partial u_3}{\partial x_3}}\right) \tag{3.63}$$

Integrating equation (3.63) up to time t, we acquire:

$$\begin{aligned}\int_0^t \frac{d}{dt}\overline{\rho}\overline{u_2^{'}u_2^{'}}dt = &- \int_0^t \frac{1}{\gamma\overline{p}}\frac{d}{dt}\overline{p^{'}p^{'}}dt - 2\int_0^t \overline{p^{'}\frac{\partial u_1}{\partial x_1}} \\ &- 2\int_0^t \overline{p^{'}\frac{\partial u_3}{\partial x_3}}.\end{aligned} \tag{3.64}$$

The time-integrated behavior of the pressure strain correlation tensor has been investigated by Lavin et al. [10]. One key discovery was the magnitudes of time integrated values of Π_{33} and Π_{22} for different initial modal Mach numbers tend toward the same asymptotic values at late times when evaluated against the time integrated behavior of Π_{11}:

$$\frac{\int_0^t \Pi_{22} dt}{\int_0^t \Pi_{11} dt} \approx -\frac{1}{2} \quad and \quad \frac{\int_0^t \Pi_{33} dt}{\int_0^t \Pi_{11} dt} \approx 0. \tag{3.65}$$

Based on these findings, the late time behavior of Π_{11} and Π_{33} are expressed as:

$$\int_0^t \frac{d}{dt}\overline{\rho}\overline{u_2' u_2'} dt = -\int_0^t \frac{1}{\gamma \overline{p}} \frac{d}{dt}\overline{p' p'} dt + 4\int_0^t \overline{p' \frac{\partial u_2}{\partial x_2}'}. \tag{3.66}$$

Utilizing (3.62), equation (3.66) reduces to:

$$\int_0^t \frac{d}{dt}\overline{\rho}\overline{u_2' u_2'} dt = -\int_0^t \frac{1}{\gamma \overline{p}} \frac{d}{dt}\overline{p' p'} + 2\overline{\rho}\int_0^t \frac{d\overline{u_2' u_2'}}{dt} dt \tag{3.67}$$

Integrating and neglecting the initial values of the pressure and velocity moments and change in $\overline{p}$, we obtain:

$$\overline{\rho}\overline{u_2' u_2'} \approx \frac{1}{\gamma \overline{p}}\overline{p' p'} \Rightarrow \frac{\overline{p' p'}}{\overline{u_2' u_2'}\gamma \overline{p}\overline{\rho}} \approx 1. \tag{3.68}$$

This implies, given adequate time, compressible homogeneous shear flows will achieve a balance between the pressure fluctuations and dilatational kinetic energy. In Figure III.18 we present the computational results of the periodic shear cases against the constant shear case and equi-partition is achieved. The steady shear case shows a clear evolution towards the pressure-dilatational energy balance. However, the unsteadiness in the periodic shear cases seems to require more time to reach equi-partition for higher frequencies.

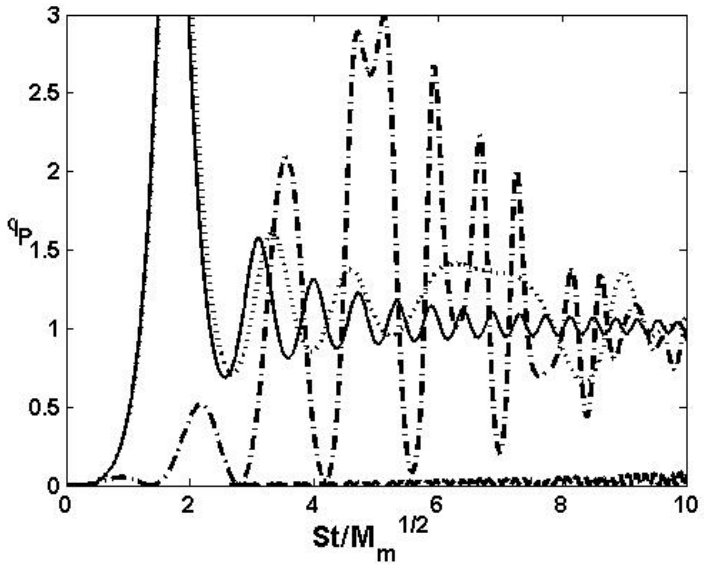

Figure III.18. Equi-partition between dilatational kinetic energy, $\overline{u_2u_2}/2$, and pressure fluctuations, $\overline{p'p'}$, for initial modal Mach number $M_m = 5$and various frequencies. $\phi_p \equiv \overline{u_2u_2}/c_p(\overline{T}-\overline{T_0})$. $(\omega = 0S)$ **:** $-$, $\omega = S/10$ **:** $\cdots$,$\omega = 1S$ **:** $(- \cdot -)$, $\omega = 10S$ **:** $(--)$.

III.E. Conclusions

The effect of unsteady-shear forcing on a compressible homogeneous turbulence flow field is examined at the rapid distortion limit. The objective is to investigate the stability characteristics of such flows and distinguish the combined effects of unsteady forcing and compressibility from the individual influences. The study focuses on flow-thermodynamics interactions under unsteady-shear forcing and the consequent influence on velocity field.

The study commences with a simplified inviscid linear analysis of the perturbation pressure equation. Two regimes of pressure behavior are identified in the case unsteady shear in contrast to three in the steady case. The first regime corresponds to

shear timescale being much smaller than the acoustic timescale. This regime characterized by very little flow-thermodynamics interactions leading to monotonic growth of the perturbation velocity unencumbered by pressure field. In the second regime, the pressure and shear timescales are of the same order of magnitude. This leads to a strong coupling between pressure and velocity fields. It is important to recognize that this pressure-velocity coupling is very different from that in incompressible flow which is characterized by the acoustic timescale being much more rapid than that of the flow field leading to the Poisson equation for pressure. In the second compressible regime, the shear-normal velocity perturbation and pressure are coupled as in a harmonic oscillator. This leads to oscillations in shear stress, which yields nearly net zero production over a cycle, thus stabilizing the flow. Beyond the second regime, the unsteady and steady shear cases differ. In the steady case, the pressure-field frequency keeps increasing to magnitudes much larger than the shear frequency. At this stage, the steady case transitions to a third incompressible-like regime, wherein the perturbations grow. In the unsteady case it can be shown that the pressure-field frequency is confined to smaller values and the second regime persists even at long times.

In summary, the compressible homogeneous turbulence field subject to unsteady shear forcing appears to be stabilized unconditionally. Such a field experiences neither the third-regime growth of the steady compressible case, nor the resonant growth of unsteady incompressible field.

CHAPTER IV

DIRECT NUMERICAL SIMULATION OF SMALL PERTURBATION GROWTH IN COMPRESSIBLE KOLMOGOROV FLOW

Investigation on the effects of inhomogeneity in high-speed shear flows is an area of research demanding attention. Kolmogorov flow, a spatially periodic mean flow, is ideal for investigating inhomogeneity in a flow field. Early Kolmogorov flow studies focused on analysis of the governing equations [23], simulations of linearized equations [24–27] and direct numerical simulation [28–30]. In these studies, authors considered both bounded and unbounded flows [24], the effect of unsteadiness [23] and viscosity [25, 28]. A majority of Kolmogorov flow studies have investigated the incompressible regime and although conclusions vary depending on the focus of the study, they agree that the normal modes exhibit nonoscillatory growth [23–25]. Several of the studies suggest that the inhomogeneity in the flow can have a stabilizing effect even at low speeds [25, 26, 28]. To date, only one study exists that investigates the effect of compressibility on Kolmogorov flow [31]. The study presented in this chapter will focus on high-speed Kolmogorov flow to examine the combined effects of compressibility and inhomogeneity on stability.

IV.A. Governing Equations

The compressible, ideal-gas Navier-Stokes equations form the basis of the DNS study:

$$\frac{\partial \rho}{\partial t} + \frac{\partial (\rho u_i)}{\partial x_i} = 0, \tag{4.1}$$

$$\frac{\partial (\rho u_i)}{\partial t} + \frac{\partial (\rho u_i u_j + p\delta_{ij})}{\partial x_j} = \frac{\partial \sigma_{ij}}{\partial x_j}, \tag{4.2}$$

$$\frac{\partial E}{\partial t} + \frac{\partial [(E+p)u_i]}{\partial x_i} = \frac{\partial (\sigma_{ij} u_j)}{\partial x_i} - \frac{\partial}{\partial x_i}\left(\kappa_t \frac{\partial T}{\partial x_i}\right). \tag{4.3}$$

The viscous stress tensor σ_{ij} is given by a constitutive relation:

$$\sigma_{ij} = \mu \left[\frac{\partial u_i}{\partial x_j} + \frac{\partial u_j}{\partial x_i} + \lambda \delta_{ij} \frac{\partial u_k}{\partial x_k}\right], \tag{4.4}$$

and the thermodynamic pressure p is given by the ideal gas law:

$$p = \rho R T, \tag{4.5}$$

where μ is the coefficient of dynamic viscosity, κ_t is the thermal conductivity, $\lambda = -(2/3)\mu$ is the second viscosity coefficient and R is the gas constant.

IV.A.1. Reynolds stresses

For the purpose of analyzing important turbulent quantities, the instantaneous fields are decomposed into mean/background and fluctuation/perturbation components:

$$q = \bar{q} + q'. \tag{4.6}$$

Some key quantities analyzed in turbulent flows are the Reynolds stresses and turbulent kinetic energy. The Reynolds Stress evolution equation (RSEE) stems from

the Navier-Stokes equations with the familiar form:

$$\frac{d\overline{u_i'u_j'}}{dt} = P_{ij} + R_{ij} - \epsilon_{ij} - \frac{\partial}{\partial x_k}T_{kij}, \tag{4.7}$$

where P_{ij} is the production tensor defined as:

$$P_{ij} = -\overline{u_i'u_k'}\frac{\partial\overline{U_j}}{\partial x_k} - \overline{u_j'u_k'}\frac{\partial\overline{U_i}}{\partial x_k}, \tag{4.8}$$

R_{ij} is the pressure-rate-of-strain tensor:

$$R_{ij} = \overline{\frac{p'}{\rho}\left(\frac{\partial u_i'}{\partial x_j} + \frac{\partial u_j'}{\partial x_i}\right)}, \tag{4.9}$$

ϵ_{ij} is the dissipation tensor:

$$\epsilon_{ij} = 2\nu\overline{\frac{\partial u_i'}{\partial x_k}\frac{\partial u_j'}{\partial x_k}}, \tag{4.10}$$

and T_{kij} is the Reynolds-stress flux tensor which has three components:

$$\begin{aligned} T_{kij} &= T_{kij}^{(u)} + T_{kij}^{(p)} + T_{kij}^{(\nu)} \\ &= \overline{u_i'u_j'u_k'} + \frac{1}{\rho}\overline{u_i'p'}\delta_{jk} + \frac{1}{\rho}\overline{u_j'p'}\delta_{ik} - \nu\frac{\partial\overline{u_i'u_j'}}{\partial x_k}. \end{aligned} \tag{4.11}$$

The evolution of turbulent kinetic energy is also governed by a reduced form of (4.7) since $k = \frac{1}{2}\overline{u_i'u_i'}$:

$$\frac{dk}{dt} = \frac{d\overline{u_i'u_i'}}{dt} = P_{ii} + R_{ii} - \epsilon_{ii} - \frac{\partial}{\partial x_k}T_{kii}. \tag{4.12}$$

Each term in the RSEE equation encompasses different physical processes in the evolution of turbulence in the flow field. Investigations of individual terms and analysis of (4.7) is crucial to understanding the effect of compressibility.

IV.A.2. Linear analysis

To begin an in depth analysis of the governing equations (4.1-4.3) and (4.7), the mean/background and perturbation/fluctuation field equations must be established.

After applying basic averaging rules to equations (4.1-4.3), the mean flow field evolves according to the following equations:

$$\frac{\partial \overline{\rho}}{\partial t} + \overline{U_j}\frac{\partial \overline{\rho}}{\partial x_j} = -\overline{\rho}\frac{\partial \overline{U_j}}{\partial x_j} - \frac{\partial \overline{\rho' u_j'}}{\partial x_j}, \tag{4.13}$$

$$\frac{\partial \overline{U_j}}{\partial t} + \overline{U_j}\frac{\partial \overline{U_i}}{\partial x_j} = -\overline{u_j'\frac{\partial u_i'}{\partial x_j}} - \frac{1}{\overline{\rho}}\frac{\partial \overline{p}}{\partial x_i} + \frac{1}{(\overline{\rho})^2}\overline{\rho'\frac{\partial p'}{\partial x_i}} - \frac{\overline{(\rho')^2}}{(\overline{\rho})^3}\frac{\partial \overline{p}}{\partial x_i}, \tag{4.14}$$

$$\frac{\partial \overline{p}}{\partial t} + \overline{U_j}\frac{\partial \overline{p}}{\partial x_j} = -\overline{u_j'\frac{\partial p'}{\partial x_j}} - \gamma\overline{p}\frac{\partial \overline{U_j}}{\partial x_j} - \gamma\overline{p'\frac{\partial u_j'}{\partial x_j}}, \tag{4.15}$$

Note that we utilized the ideal gas law in the energy equation (4.15) to reduce the number of thermodynamic properties and ignored the viscous terms. To obtain the governing equations for the perturbation field, the mean/background field equations, (4.13-4.15), are subtracted from the instantaneous field, (4.1-4.3). Before we present the fluctuating field equations for analysis, we will introduce some flow field assumptions that are common when examining unbounded shear flows.

For Kolmogorov flow, we impose a mean or background spatially periodic velocity gradient in the flow normal direction (seen in figure IV.1):

$$\frac{\partial \overline{U_i}}{\partial x_j} = \begin{bmatrix} 0 & S_0\cos(x_2) & 0 \\ 0 & 0 & 0 \\ 0 & 0 & 0 \end{bmatrix}. \tag{4.16}$$

In a similar fashion to homogeneous shear flow, this mean flow field infers that $\frac{\partial \bar{p}}{\partial x_i} = 0$ and $\frac{\partial \bar{U}_i}{\partial x_i} = 0$. In the linear limit, we ignore any terms with higher than first order fluctuation/perturbation variables. This implies:

$$\overline{\rho} \approx \overline{\rho}(0); \quad \overline{T}(t) \approx \overline{T}(0) \text{ and } \overline{p}(t) \approx \overline{p}(0). \tag{4.17}$$

Applying the above assumptions to the fluctuation/perturbation field equations,

yields:

$$\frac{d\rho'}{dt} = -\overline{\rho}\frac{\partial {u_k}'}{\partial x_k}, \tag{4.18}$$

$$\frac{d{u_i}'}{dt} = -{u_k}'\frac{\partial \overline{U_i}}{\partial x_k} - \frac{1}{\overline{\rho}}\frac{\partial p'}{\partial x_i}, \tag{4.19}$$

$$\frac{dp'}{dt} = -\gamma\overline{p}\frac{\partial {u_k}'}{\partial x_k}. \tag{4.20}$$

Through application of the previous assumptions to equations (4.7) and (4.12), the evolution equations for Reynolds stresses and turbulent kinetic energy for linearized, inviscid shear flows is given by:

$$\frac{d\overline{u_i' u_j'}}{dt} = P_{ij} + R_{ij}, \tag{4.21}$$

$$\frac{dk}{dt} = P_{11} + R_{ii}, . \tag{4.22}$$

IV.B. Numerical Simulation and Validation

For this study, direct numerical simulations were performed using the gas-kinetic method (GKM). The GKM is a finite volume based numerical scheme that exploits the Bhatnagar-Gross-Krook collision operator to solve the Boltzmann equation. The kinetic Boltzmann equation describes the evolution of a fluid particle distribution function. The conservative flow variables, such as density, velocity and energy, are calculated integrating the distribution function. The gas-kinetic equation is a first order integro-partial differential equation with a linear advection term. Details of the numerical solution for the gas kinetic equations can be found in [32–36].

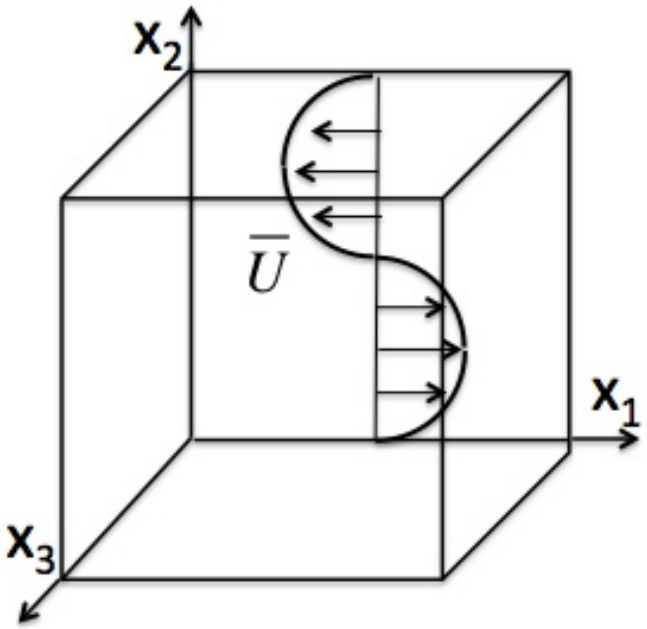

Figure IV.1. Schematic of the mean/background field setup.

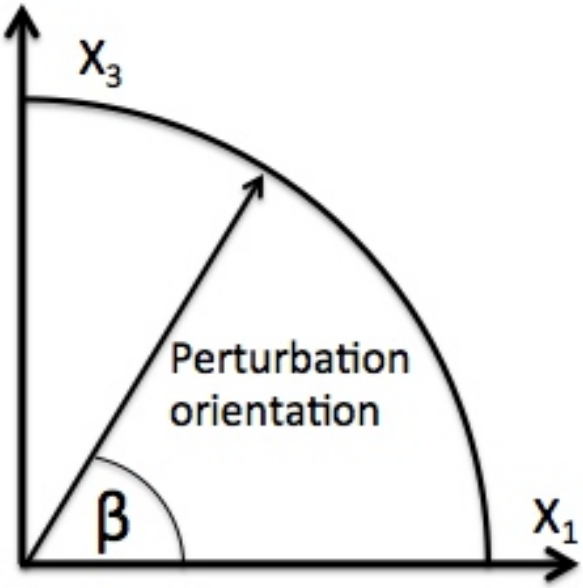

Figure IV.2. A typical oblique mode in modal simulations.

IV.B.1. Initial field setup

The computational domain utilized for the majority of the simulations is a cubic box of dimension $l = 2\pi$. The box is discretized into $N_1 \times N_2 \times N_3$ cells with $N_1 = N_2 = N_3 = 256$ along the x_1, x_2 and, x_3 directions respectively. We apply a spatially periodic shear in u_1 along the x_2 direction such that the gradient of the mean flow field is $\bar{U}_{i,j} = S_0 \cos(x_2)\delta_{i1}\delta_{2j}$ where S_0 is the maximum shear rate. The mean field setup is presented in figure IV.1. Since the shear rate is periodic along the flow normal direction, we can apply periodic boundary conditions along all directions.

In DNS and RDT studies of homogeneous shear flows, the initial gradient Mach number is identified as the main compressibility parameter:

$$M_{g,0} = \frac{S\ell_0}{a_0}, \tag{4.23}$$

where S is the shear magnitude(initial mean velocity gradient), ℓ_0 is an integral length scale and a_0 is the speed of sound based on mean temperature. For Kolmogorov flow, the shear magnitude at the inflection points in the mean flow will be used to determine this compressibility parameter.

The simulations presented in this paper consist of two different initial field setups. One set of initial conditions imposes a single wave mode perturbation oriented within the streamwise (x_1) and spanwise (x_3) plane to study the influence of obliqueness angle. A schematic of this initial setup can be seen in figure IV.2. The reason for choosing to orient the wave vectors is the $x_1 - x_3$ plane is described in detail in Kumar et al. [11] and is evident upon examination of the wave number evolution

equation:

$$\frac{d\kappa_i}{dt} = -\kappa_j \frac{d\overline{U}_j}{dx_i}. \tag{4.24}$$

From equations (4.16) and (4.24), the individual components of the wave vector evolve according to:

$$\kappa_1(t) = \kappa_1(0) \equiv \kappa_1^0; \quad \kappa_2(t) = \kappa_2(0) - \kappa_1(0) S_0 \cos(x_2) t; \quad \kappa_3(t) = \kappa_3(0) \equiv \kappa_3^0. \tag{4.25}$$

The angle β seen in figure IV.2, measures the obliqueness to the streamwise direction. For oblique modes, the effective shearing rate experienced by individual perturbations at different vertical planes is defined as:

$$S^* = S_0 \cos(x_2) \cos(\beta), \tag{4.26}$$

and the corresponding effective gradient Mach number:

$$M_g^* \equiv \frac{S^* \ell}{a} = M_{g0} \cos(x_2) \cos(\beta) = \frac{S^*}{a_0 |\kappa(0)|}. \tag{4.27}$$

For modal analysis, the evolution of the perturbation is directly dependent on the wave vector orientation and vertical location of each plane.

The second type of initial condition is constructed from a collection of three dimensional, random, isotropic and solenoidal ($\nabla \cdot \mathbf{u} = 0$) wave mode perturbations. The initial energy spectra is restricted to wavenumbers in the range $\kappa \in [\kappa_{min}, \kappa_{max}]$. The velocity field is periodic and satisfies a one-dimensional energy spectra [37–39]:

$$E(\kappa, 0) = \frac{\hat{u}_i \hat{u}_i^*}{4\pi\kappa^2} = A\kappa^4 e^{-B\kappa^2}, \quad \kappa \left(= \sqrt{\kappa_1^2 + \kappa_2^2 + \kappa_3^2} \right) \in [\kappa_{min}, \kappa_{max}], \tag{4.28}$$

where $B = 0.54$, $\hat{u}_i$ is the Fourier amplitude and $\hat{u}_i^*$ is its complex conjugate and κ_1, κ_2 and κ_3 are the components of the wave number vector. The detailed steps

for generating such a field are given in [36, 38–40]. The value of A is calculated to obtain the prescribed initial fluctuation intensity or equivalently the initial turbulent Mach number M_{t0}. The kinematic viscosity ν is chosen to achieve an initial Taylor microscale Reynolds number $Re_{\lambda 0}$. The initial temperature and density fields are chosen to be uniform instead of the isentropic state proposed by [41]. This choice of initial thermodynamic flow field variables has been utilized in a recent study [11] and validated against previous DNS studies.

Recent studies have utilized this DNS approach with the same GKM scheme for other types of shear flow [11, 42]. For compressible homogenous shear flow, [11] validated this numerical approach against a previous DNS study by Sarkar [4]. Excellent agreement was seen between the two DNS approaches when examining the components of the anisotropy tensor and the correlation coefficient. In another study, bounded shear flows were also examined using this DNS approach by Xie & Girimaji [42]. In their study, Xie & Girimaji [42] prove that the DNS approach being utilized in this study, is valid for both low-speed and infinite Mach-number Poiseuille flow. Based on these previous studies, this approach is sufficiently validated for this Kolmogorov flow investigation.

As a first verification step of the applicability of the numerical scheme to Kolmogorov flow, we examine the budget of the Reynolds stress evolution equation (4.7). Both sides of equation (4.7) are computed directly from the simulation data and compared at specific time instances and presented in figure IV.3. By comparing both sides of the equation, we seek to exhibit the numerical precision. Nearly perfect agreement is seen at all time instances, thus showing that the numerical scheme is

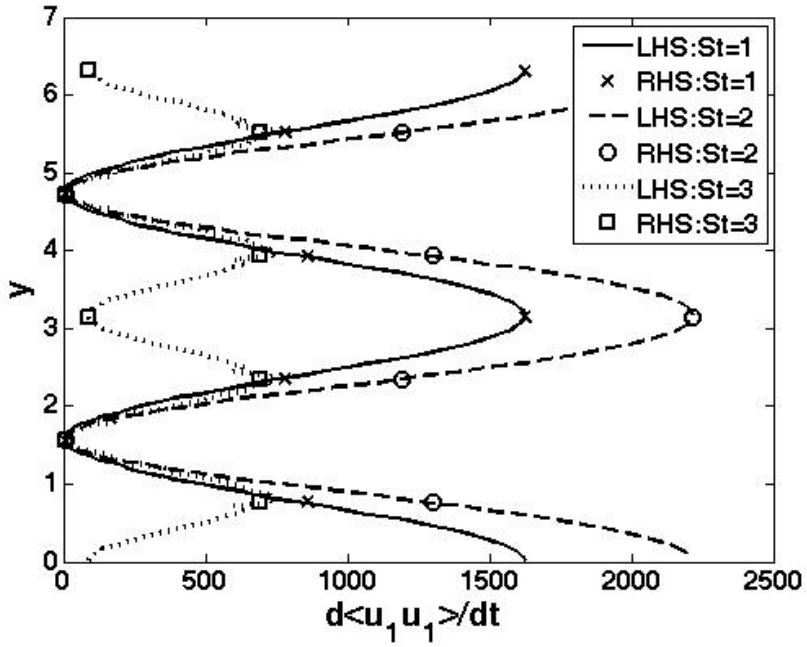

Figure IV.3. Validation of our DNS method where the right and left hand sides of the Reynolds Stress Evolution show near perfect agreement at several specific times for gradient Mach numbers($M_g = 5$).

appropriate for this inhomogeneous study.

IV.B.2. Relevant previous studies and preliminary results

Before we present our results of single mode perturbations for Kolmogorov flow, we summarize recent studies of single-mode instability in different high-speed shear flows. The importance of investigating the evolution of individual small perturbations in high-speed shear flow was first shown in [11]. Upon examination of the wave equation for pressure in homogeneous shear flows [9, 11] , it is evident that the evolution of the pressure field is heavily influenced by the orientation of the initial wave number vector in the streamwise-spanwise plane (x_1x_3 plane in figure IV.2).

The single mode study [11] showed a large increase in dilatational energy when the initial perturbation is oriented close to the streamwise direction. When oriented along or closer to the spanwise direction, insignificant dilatational energy was observed and the perturbation evolved nearly independent of the initial gradient Mach number (or shearing magnitude). In a similar study of individual perturbations in high-speed channel flow, [42] found similar results. These studies present a new parameter, β_{crit}, which demarcates the orientation in the streamwise-spanwise plane where the effective gradient Mach number transitions from a supersonic to a subsonic value.β_{crit} is defined as:

$$\beta_{crit} = \cos^{-1}\left(\frac{1}{M_{g,0}}\right). \tag{4.29}$$

In these studies [11, 42], this parameter demarcates two regions of the evolution of perturbations. At $\beta < \beta_{crit}$, the modes appear to be stable since they experience suppression of the growth rate of perturbation evolution due to the effective gradient Mach number being above unity . For $\beta > \beta_{crit}$, which are considered the subsonic modes, the growth rate suppression disappears and the evolution becomes nearly independent of the initial gradient/modal Mach number indicating these modes are unstable. As these two studies both examine different types of shear flows, it is reasonable to anticipate a similar behavior in Kolmogorov flows.

Simulation of Kolmogorov flow permits the study of ideal flow field inhomogeneity by forcing a range of shear rates within the same grid. Each individual plane in the flow normal direction can be conceptualized as a uniform/homogeneous shear flow with a unique shear magnitude. Using DNS for this study allows us to gain insight on turbulent transport and dissipation effects in non-ideal inhomogeneous flows.

In figures IV.4 and IV.5, the evolution of turbulent kinetic energy in compressible homogenous shear and compressible Kolmogorov flow subject to a collection of initial perturbation modes are presented. The stabilizing nature of compressibility due to the change in nature of pressure [9, 11] is clearly demonstrated in figure IV.4. Even with the addition of non-local instabilities found in Kolmogorov flow, compressibility still exhibits a stabilizing influence on flow field evolution (figure IV.5). Further, it can be seen that inhomogeneity is stabilizing even in compressible flows [25, 26, 28]. Since we already established that the effective gradient Mach number and shear rate for Kolmogorov flow have an additional factor of being dependent on the flow normal location, β_{crit} for individual planes in this study is defined as:

$$\beta_{crit} = \cos^{-1}\left(\frac{1}{M_{g,0}\cos(x_2)}\right). \tag{4.30}$$

The remainder of this chapter will be dedicated to examining single mode perturbation evolution in compressible Kolmogorov flow to improve understanding of the overall effect of inhomogeneity in free shear flows.

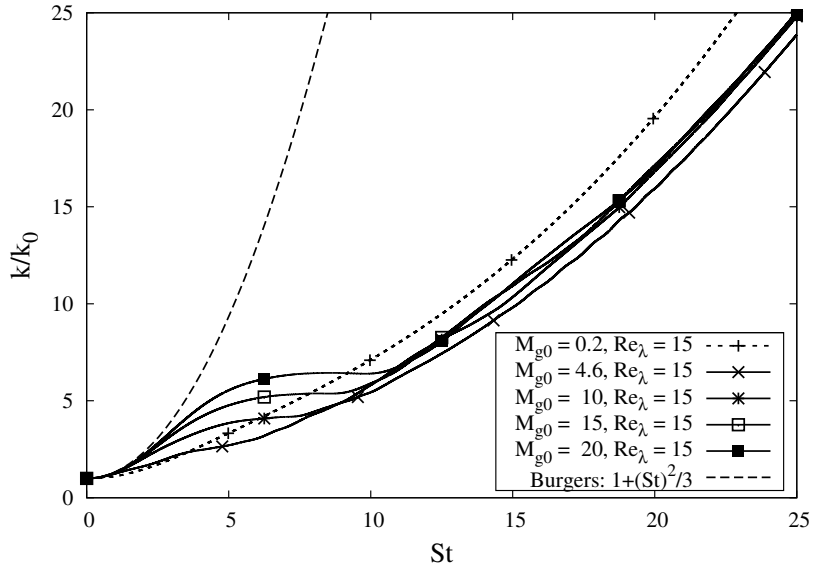

Figure IV.4. Evolution of turbulent kinetic energy for a collection of modes in homogeneous shear flow for various initial gradient Mach numbers(M_g). Figure previously seen in the doctoral dissertation of Gaurav Kumar [43].

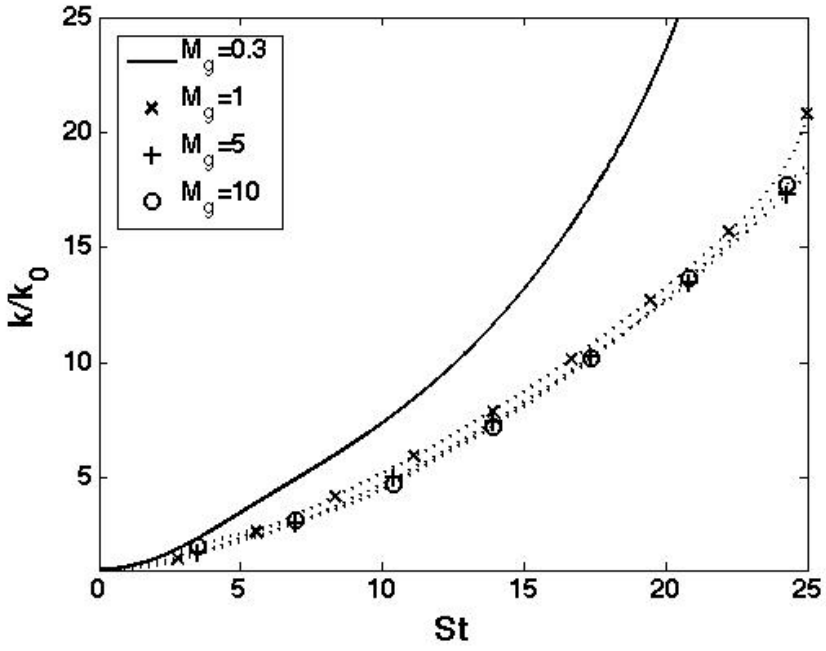

Figure IV.5. Evolution of turbulent kinetic energy for a collection of modes in Kolmogorov flow for various initial gradient Mach numbers(M_g).

IV.C. Single Mode Simulations

To fully comprehend the effect of inhomogeneity on the flow field hysics, individual perturbation modes will be examined. Volume averaged quantities will be used to determine the influence of perturbation mode orientation in the streamwise-spanwise plane. Volume averaged quantities will also be used to investigate the influence of initial gradient Mach number at fixed obliqueness angles to determine if a stability boundary classification , similar to that found in [11], is present. Finally, streamwise-spanwise planar averages will be taken in the flow normal direction to investigate the inhomogeneity effects on different perturbations.

IV.C.1. Influence of perturbation obliqueness, β

As in the compressible homogeneous shear study, the obliqueness angle, β, determines the effective Mach number experienced by a perturbation oriented in the streamwise-spanwise plane. Consequently, β also strongly influences the evolution of the turbulent kinetic energy within the flow field. Figures IV.6 and IV.7 demonstrate the influence of the obliqueness angle on two different Mach numbers. In both figures the solid line represents the streamwise ($\beta = 0$) mode, along which the perturbation experiences the maximum influence of initial gradient Mach number. Perturbations oriented closer to the streamwise direction, have a smaller growth rate implying there is a stronger stabilization effect in that region. As β increases, and the effective Mach number acting on the single perturbation decreases, a destabilization of the turbulent growth rate is exhibited. As anticipated, β_{crit} demarcates the boundary between the stable (or supersonic) and unstable (subsonic) regions of the plane. For obliqueness

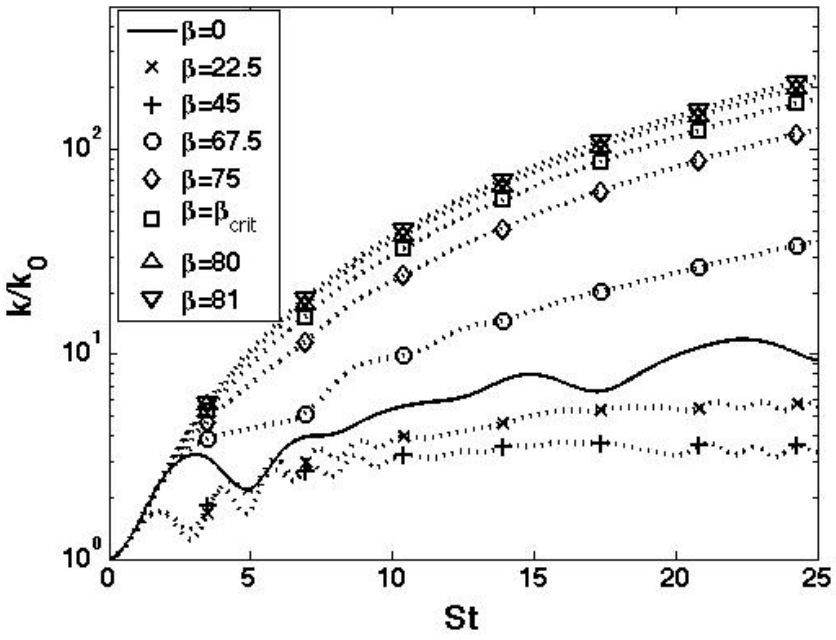

Figure IV.6. Evolution of volume averaged turbulent kinetic energy for a range of obliqueness angles,β, with an initial gradient Mach number($M_g = 5$).

angles greater than β_{crit}, all perturbations evolve along a nearly identical path. This supports the notion of a stability boundary classification similar to the homogeneous shear case but further investigation is required.

IV.C.2. Influence of Mach number

The previous subsection examined the influence of the perturbation orientation for fixed initial modal Mach numbers. Now we investigate the influence of initial modal Mach number, which acts as a measure of the amount of compressibility, at fixed perturbation orientations. Keep in mind the definition of effective shear rate and Mach number (4.26, 4.27) as we interpret the results.

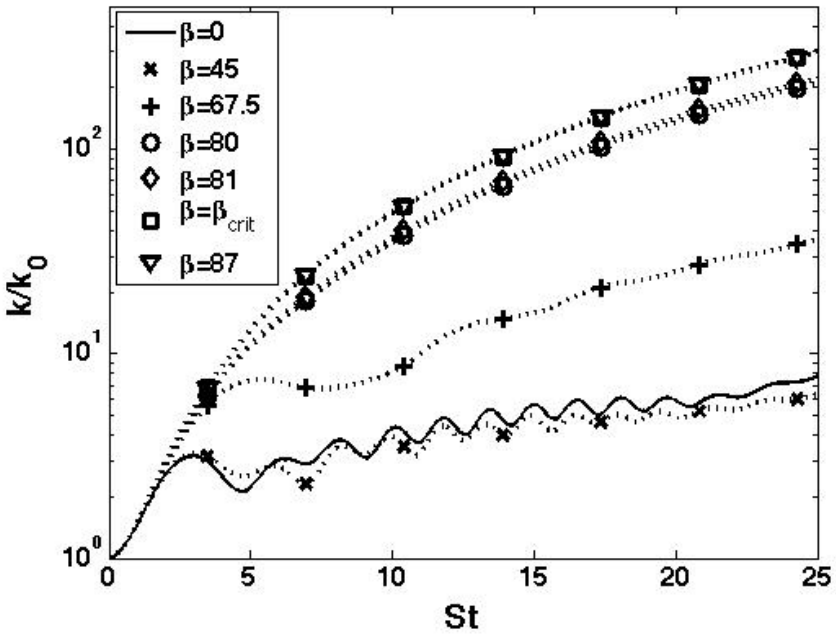

Figure IV.7. Evolution of volume averaged turbulent kinetic energy for a range of obliqueness angles,β, with an initial gradient Mach number($M_g = 10$).

IV.C.2.a. 2D or Streamwise mode: $\beta = 0$

When oriented along the streamwise direction, a perturbation experiences the full effect of the shear rate and initial Mach number. This mode is known to generate a significant amount of dilatational kinetic energy in homogeneous shear flow [11] due to the steady increase in the wavenumber vector magnitude. Figure IV.8 shows the volume-averaged evolutions of a perturbation along the streamwise direction for several initial modal Mach numbers. Since Kolmogorov flow encompasses a range of shear rates, the influence of low and zero shear planes is reflected strongly in the lowest modal Mach number case. As expected, we observe that higher compressibility (M_m) leads to higher energy levels. However, it is important to note that the perturbation evolution is asymptotically stable.

IV.C.2.b. Oblique mode: $\beta = 45$

As the perturbation orientation ventures toward the spanwise direction, noticeable differences in the evolutions are displayed. For simplicity we examine an oblique mode along the center of the streamwise-spanwise plane. Figure IV.9 shows the volume-averaged evolutions of a perturbation along $\beta = 45$ for different Mach numbers. Once again, we see increased energetics for larger M_g, but we notice that the least compressible case ($M_g = 1$) exhibits growth instead of decay as in the streamwise orientation. This can be explained by the equation for the effective Mach number (4.27). Along this orientation, a perturbation is only experiencing around 70% of the Mach number or shear strength. For the $M_g = 1$ case, the effective Mach number is in subsonic values. Therefore, we are starting to see the destabilization in

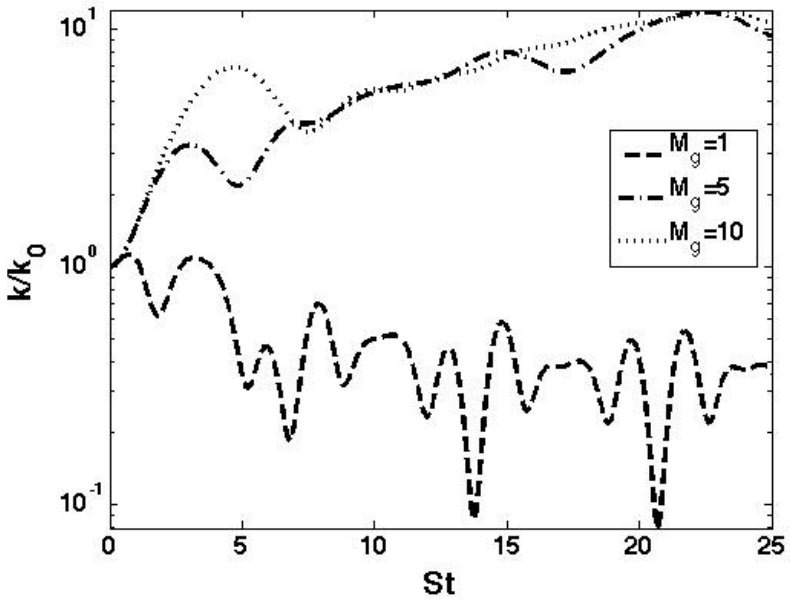

Figure IV.8. Evolution of volume averaged turbulent kinetic energy from a streamwise mode ($\beta = 0$) instability for various initial gradient Mach numbers(M_g).

growth of the perturbation for this case. The destabilization for the other cases will occur at orientations closer to the spanwise direction.

IV.C.2.c. Spanwise mode: $\beta = 90$

A perturbation oriented along or near the spanwise direction experiences a small effective shear rate and Mach number. In this thin region of the streamwise-spanwise plane, all initial gradient Mach number cases are beyond their β_{crit} values and the effective shear acting on the perturbation is well within the incompressible regime. Based on previous studies and analysis, any perturbations should evolve along the same path, regardless of initial gradient Mach number or shear rate. Figure IV.10

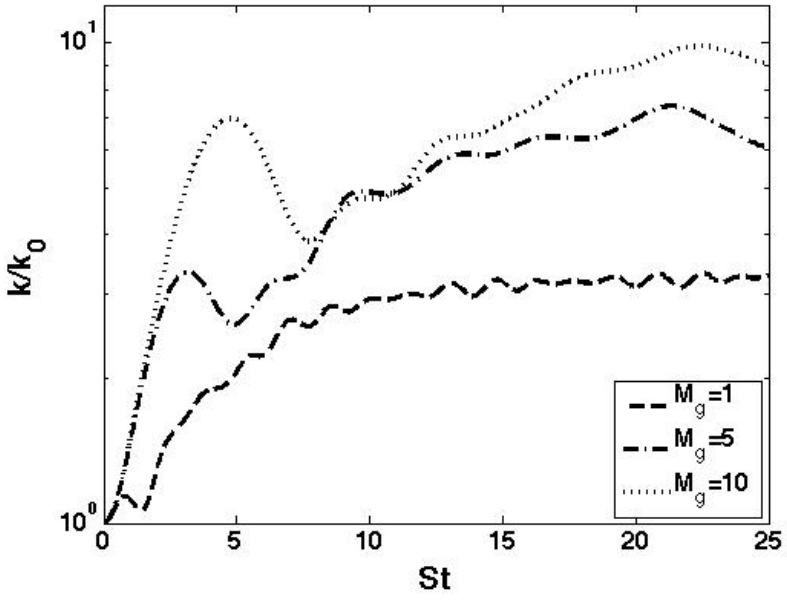

Figure IV.9. Evolution of volume averaged turbulent kinetic energy from an oblique instability ($\beta = 45$) for various initial gradient Mach numbers(M_g).

supports this claim as the perturbation oriented along the spanwise direction shows unstable growth independent of the initial Mach number value. This observation is explained by equation (4.27) which shows the effective Mach number experienced by perturbations along the spanwise mode is nearly zero.

IV.C.3. Influence of inhomogeneity

From the previous subsections, the effect of obliqueness angle, β, and initial Mach number have been established and show reasonable agreement with high-speed homogeneous shear [11] and channel flow [42] studies. Kolmogorov flow, considered an archetypal inhomogeneous shear flow, presents a unique opportunity to examine

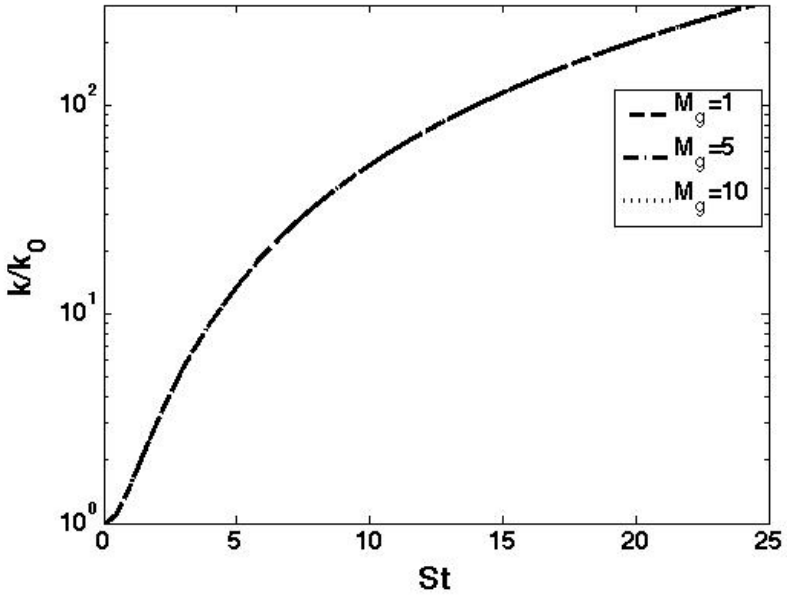

Figure IV.10. Evolution of volume averaged turbulent kinetic energy from a spanwise mode ($\beta = 90$) instability for various initial gradient Mach numbers(M_g).

the evolutions of a perturbation subject to different shear magnitudes. For the investigation that follows, we examine plane-averaged values to gain a clearer picture of the influence of inhomogeneity on individual perturbations. We will focus on three particular planes of interest shown in figure IV.11. Since DNS was used to produce these results, the behavior of the turbulent transport and dissipation terms found in the RSEE (4.7) could be deduced, especially at the low to zero shear planes.

IV.C.3.a. Maximum shear rate plane

At planes of maximum shear rate ($x_2 = 0, L/2, L$; where L is the length of the domain in the stream-normal direction) in Kolmogorov flow a perturbation is

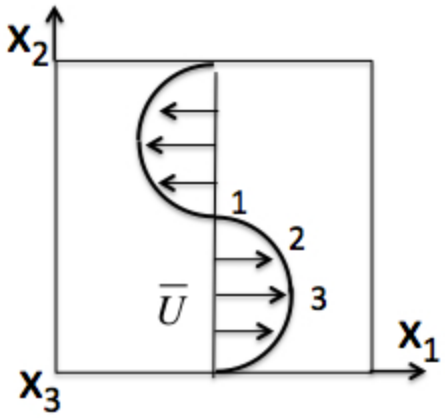

Figure IV.11. A schematic of the stream normal profile pinpointing the planes of interest: 1) the maximum shear rate location, 2) a medium shear rate location, 3) a zero shear rate location.

essentially subjected to a homogeneous shear flow. For this reason, the influence of β on a perturbation should closely resemble results from [11]. Figure IV.12 shows the evolutions of a perturbation for different Mach numbers at different obliqueness angles in the maximum shear plane. In figure IV.12a, the perturbation is oriented along the streamwise direction and the results are presented in non-dimensionalized mixed time to align the oscillations in the kinetic energy evolution of the different Mach numbers. The streamwise perturbation evolution shows strong agreement with homogeneous shear results for this mode [11], supporting the claim that the maximum shear plane is analogous to homogeneous shear flow. Any differences between this maximum shear plane perturbation evolution and that of the streamwise mode for the homogeneous study is due to the turbulent transport and dissipation among neighboring stream normal planes in Kolmogorov flow. The mixed timescale also displays evidence of the three-stage evolution common to compressible shear flows.

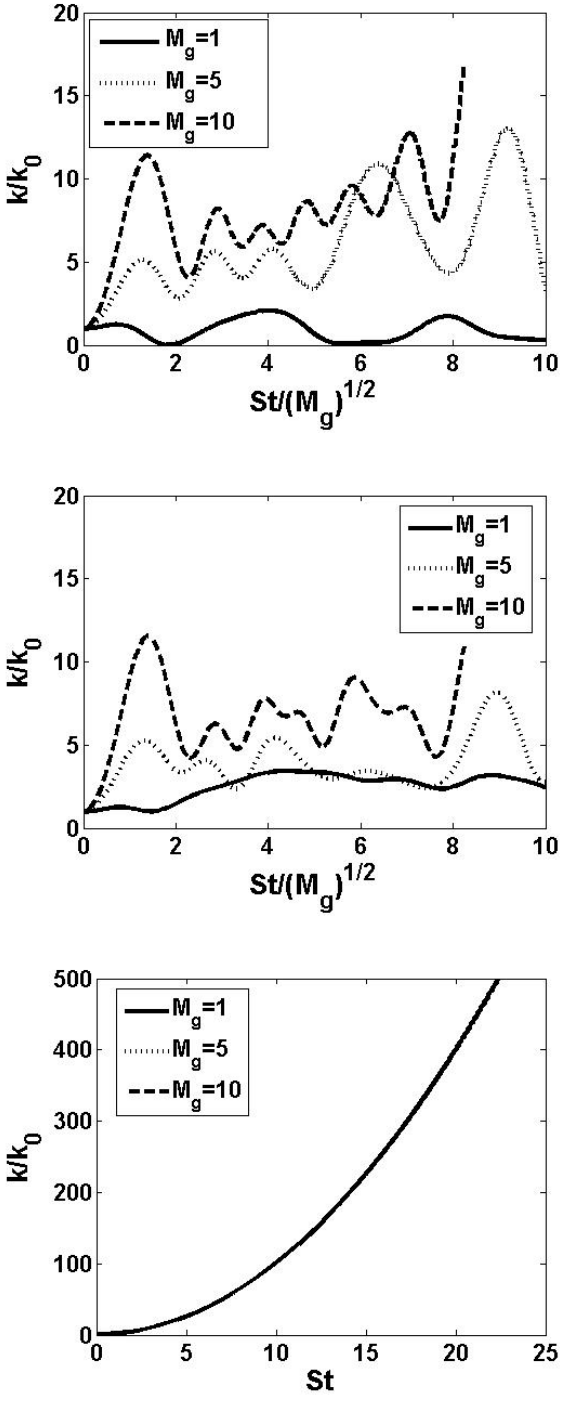

Figure IV.12. Evolution of planar averaged turbulent kinetic energy from (a) astreamwise mode instability; (b) oblique mode instability; and (c) spanwise mode instability, for various initial gradient Mach numbers(M_g) at the maximum shear location.

Figure IV.12b presents the evolutions for a perturbation oriented in the middle of the streamwise-spanwise max shear plane. Once again, we see the lowest initial Mach number case shows some destabilization similar to the volume-averaged evolution in figure IV.9. Close comparison between the streamwise and oblique mode shows a slight decrease in kinetic energy at later times. As expected from both previous studies and previous sections of this paper, the evolutions of the spanwise mode perturbation are independent of initial Mach number, seen in figure IV.12c.

IV.C.3.b. Medium shear rate plane

Medium shear plane ($x_2 = (2n-1)L/8$ for $n = 1, 2, 3, 4$) perturbation evolution give a glimpse at what most of the stream normal planes are experiencing. In these simulations where the mean/background flow is a single period sinusoidal function, there are a finite number of planes subject to the maximum shear and zero shear extremes. Figures IV.13a and IV.13b show the three-stage behavior agreement with other shear flows as well as the alignment of the evolution oscillations in the mixed timescale. The oblique mode evolutions (IV.13b) again show the slight destabilization of the low Mach number case and the decrease in energetics of the higher Mach number cases. Figure IV.13c continues the trend of showing the Mach number independence of the spanwise mode evolutions. However, we note that the spanwise evolution for the medium shear plane is at a lower growth rate than the maximum shear plane (IV.12c).

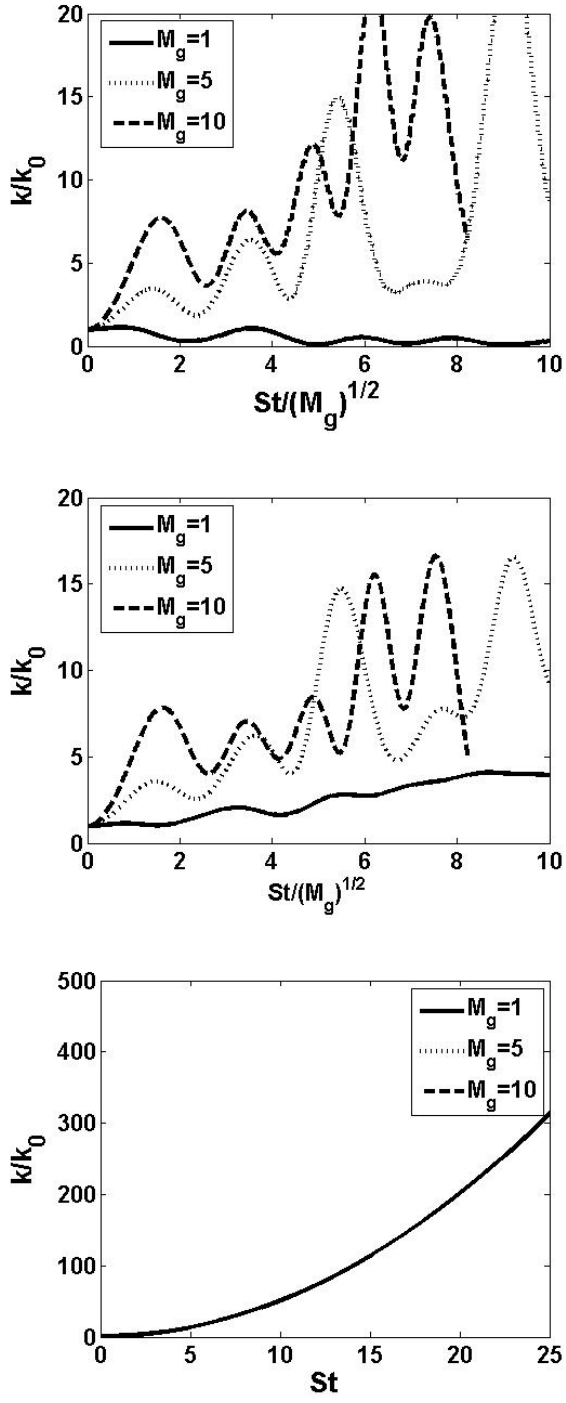

Figure IV.13. Evolution of planar averaged turbulent kinetic energy from (a) a streamwise mode instability; (b) oblique mode instability; and (c) spanwise mode instability, for various initial gradient Mach numbers(M_g)at a medium shear location.

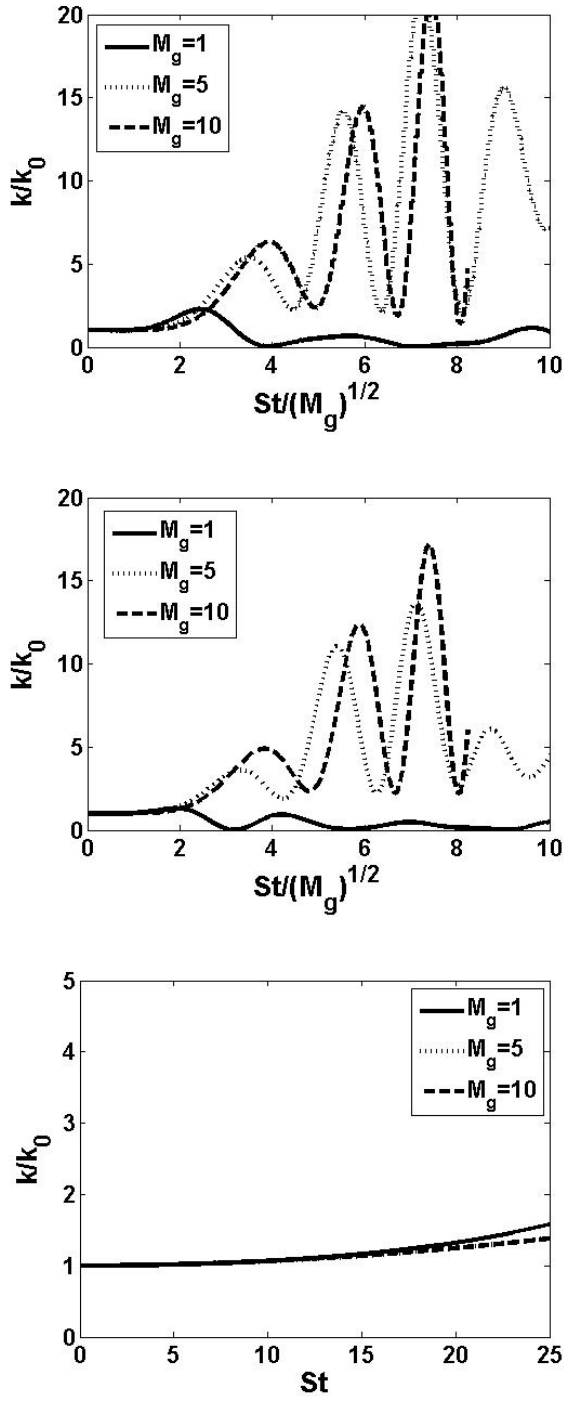

Figure IV.14. Evolution of planar averaged turbulent kinetic energy (a) a streamwise mode instability; (b) oblique mode instability; and (c) spanwise mode instability, for various initial gradient Mach numbers(M_g)at the zero shear location.

IV.C.3.c. Zero shear rate plane

Planes within Kolmogorov flow with zero shear ($x_2 = L/4, 3L/4$) allow investigations of terms in the RSEE (4.7) that are not directly dependent on the shear magnitude, such as turbulent transport and dissipation. The evolutions of a perturbation in these planes are purely determined by their interactions with their closest neighbors with nonzero shear rates. Figure IV.14 shows the evolutions of a perturbation at three distinct obliqueness angles. Both figures IV.14a and IV.14b display zero growth at early times followed by oscillatory growth and decay cycles at later times. This indicates that significant amounts of turbulent transport take time to develop in higher shear regions and the redistribution of energy by pressure and other effects will not occur immediately. In the zero shear case, figure IV.14c shows that a spanwise perturbation's growth is strongly inhibited.

Examining individual shear planes in Kolmogorov flow shows the influence of inhomogeneity is most prevalent near the zero shear region where the perturbation growth is mainly due to turbulent transport between neighboring planes. From these results, inferences can be made about the magnitude of transport at specific shear plane locations. However, to complete the investigation, we look at the evolution of the stream normal profile for key components of the RSEE (4.7).

IV.D. Reynolds Stress Evolution and Budget: Evolution of Planar Averaged Quantities

For the investigation that follows, the focus will examine different time instances of the stream normal profiles of the RSEE terms responsible for the evolution of the

turbulent shear stress, $\overline{u_1' u_2'}$. The reason for this choice is seen in equations (4.8) and (4.12) where the $\overline{u_1' u_2'}$ Reynolds stress is the main contributor to the production of turbulent kinetic energy.

IV.D.1. Kinetic energy profile

Before an investigation of the RSEE terms is performed, it is critical to compare the general evolution of the stream normal profile of turbulent kinetic energy for different perturbation modes. Figure IV.15 shows the turbulent kinetic energy profile for several time instances with an initial perturbation a) streamwise mode, b) oblique mode, and c) spanwise mode. Noting that the spanwise mode horizontal axis is nearly an order larger than the streamwise or oblique modes, all three modes present kinetic energy profiles of the same magnitude at the $St = 2$ instance. From there, the profile evolutions begin to diverge. The streamwise (a) and oblique (b) profiles develop more detail in their profiles but their maxima growth appears stable. This is likely due to all (or almost all) stream normal planes experiencing supersonic shear or Mach number values, which have already proven to exhibit stable growth. The spanwise mode (c) exhibits much larger growth rates, especially along the maximum shear planes. Understanding how the kinetic energy profiles evolve for individual perturbations can help deduce the influence of obliqueness on different terms of the RSEE.

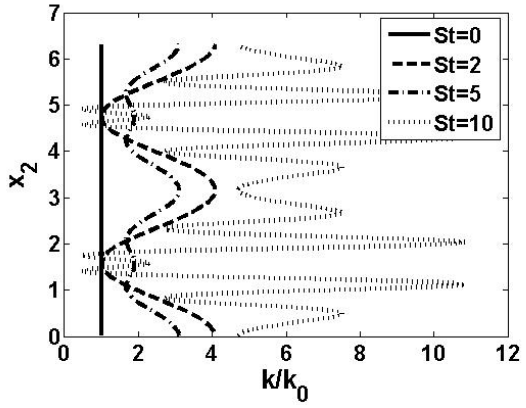

(a)

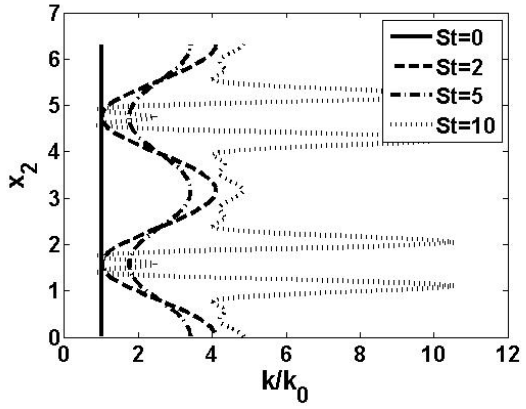

(b)

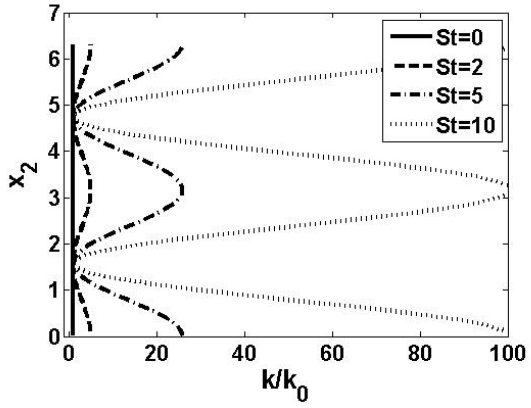

(c)

Figure IV.15. Planar averaged turbulent kinetic energy profiles for(a) a streamwise mode instability; (b) an oblique mode instability; and(c) a spanwise mode instability. $M_g = 5$**.**

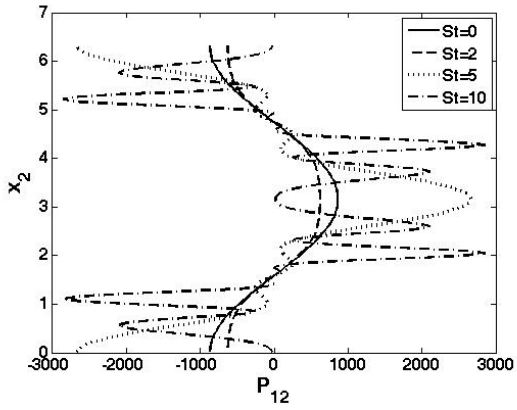

(a)

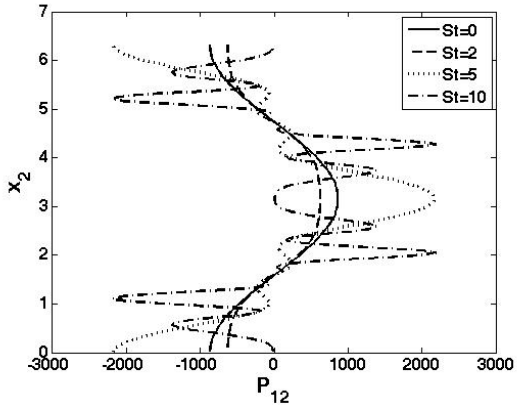

(b)

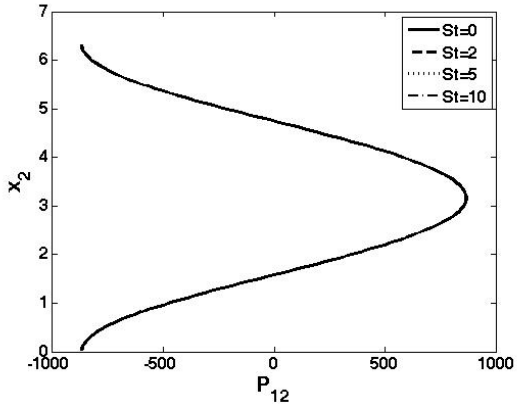

(c)

Figure IV.16. Planar averaged production (P_{12}) profiles for (a) a streamwise mode instability; (b) an oblique mode instability; and (c) a spanwise mode instability. $M_g = 5$.

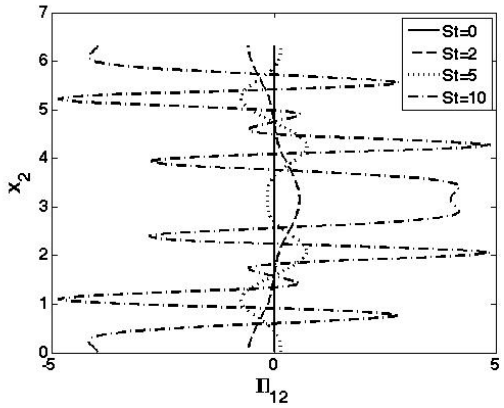

(a)

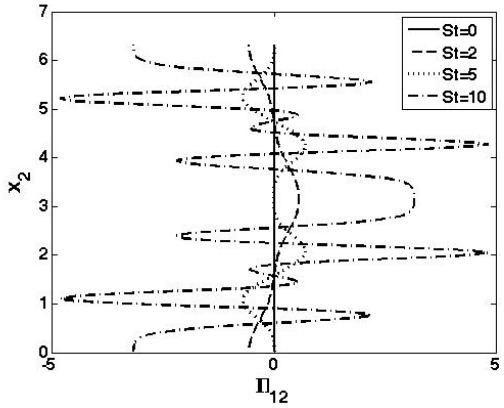

(b)

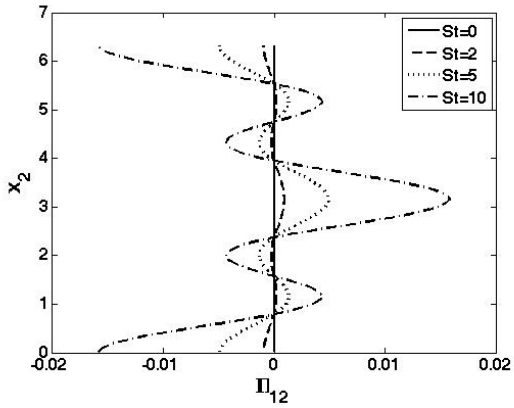

(c)

Figure IV.17. Planar averaged pressure-strain (Π_{12}) profiles for (a) a streamwise mode instability; (b) an oblique mode instability; and (c) a spanwise mode instability. $M_g = 5$.

IV.D.2. Individual terms of RSEE

IV.D.2.a. Production

The production term in the RSEE is responsible for the increase in magnitude of the perturbation and consequently the Reynolds stresses. This term transfers energy from the mean/background field to the perturbation, so in locations with large magnitudes of production, the growth of a perturbation will be large. Figure IV.16 shows the production turbulent shear production (P_{12}) for different modes. The streamwise (a) and oblique (b) modes continue to display similar profiles for early time instances. What is really of interest is figure IV.16c which shows a constant production rate inferring the growth rate of a perturbation is constant, or nearly so, along the spanwise direction. This explains the Mach number independent behavior along this mode. With the knowledge of how the obliqueness influences production, we next examine how the energy is distributed among different components.

IV.D.2.b. Pressure-Strain Correlation (Π_{12})

The role of the pressure-strain correlation is to redistribute the energy among different components to impose the divergence-free constraint on the velocity field. Figure IV.17 shows the pressure-strain stream normal profiles for several time instances at fixed obliqueness angles. Again, the streamwise (a) and oblique (b) modes are similar in features. The spanwise mode (c) for this term shows a gradual increase in strength of the redistribution term at locations of maximum shear. At zero shear locations, this term is nearly zero for all modes. In linear theory, production and pressure-strain encompass almost all the details of the kinetic energy evolution. In

this DNS study, there are still terms that need to be investigated.

IV.D.2.c. Turbulent Transport

The Reynolds stress flux is better known as the turbulent transport term as it can exchange energy between neighboring planes in Kolmogorov flow. We already mentioned turbulent transport in the previous sections, which examined the influence of inhomogeneity. Figure IV.18 shows the Reynolds stress flux profiles at different times. The streamwise (a) and oblique (b) mode show complex profiles form, but the large magnitude flux values that are found between the zero and maximum shear planes are clearly visible. It is also important to note that the magnitudes of this flux or turbulent transport profile is near zero for early times and only the $St = 10$ profile has significant values. This supports earlier results when we examined the zero shear case that suggested the turbulent transport term is insignificant at early times. There is one final term of the RSEE that must be examined to complete the investigation.

IV.D.2.d. Dissipation

In the RSEE equation, dissipation behaves like a sink term which uses viscous action to transforms kinetic energy into internal energy. In comparisons of DNS [11] versus linear methods [9] of high-speed homogeneous shear, dissipation is responsible for the reduced kinetic energy growth rates at later times. Figure IV.19 shows stream normal dissipation profiles for specified perturbation orientations. This is the only term in the RSEE (4.7) that shows a distinction in the profile evolution between

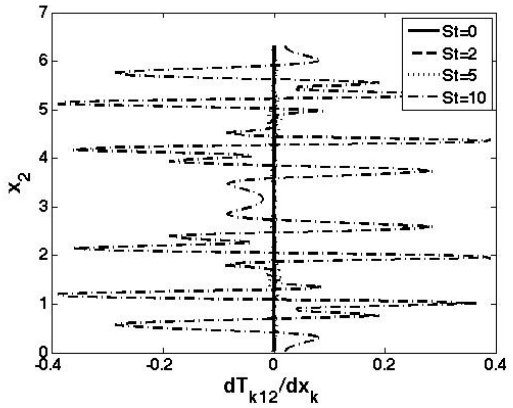

(a)

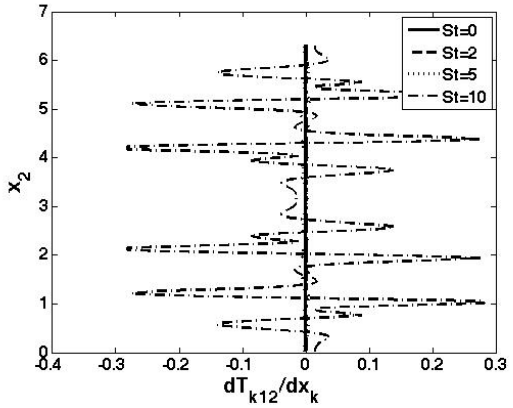

(b)

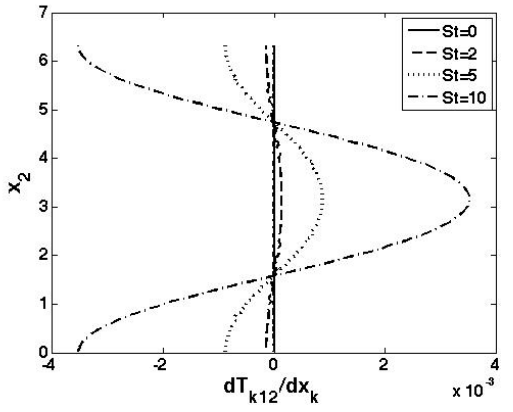

(c)

Figure IV.18. Planar averaged turbulent transport profiles for (a) a streamwise mode instability; (b) an oblique mode instability; and (c) a spanwise mode instability. $M_g = 5$.

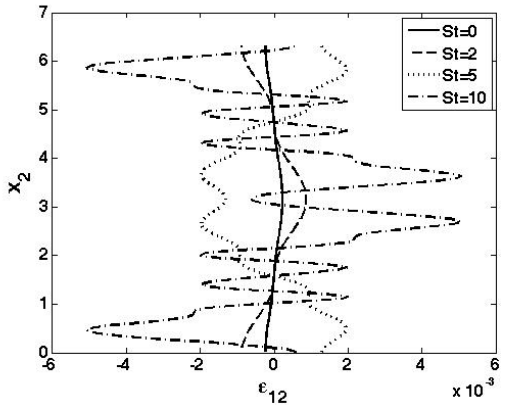

(a)

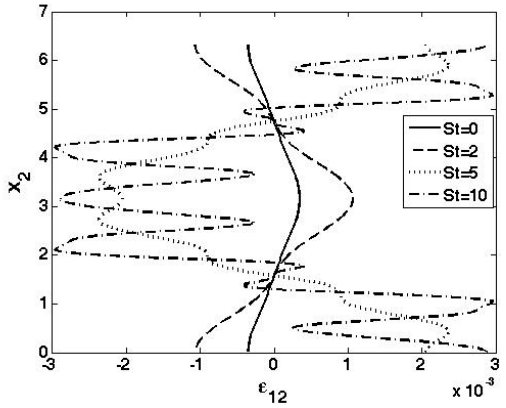

(b)

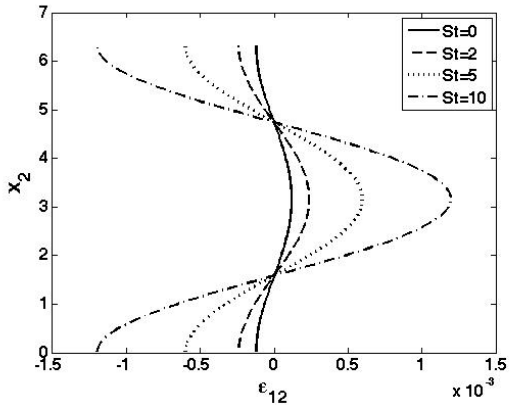

(c)

Figure IV.19. Planar averaged turbulent transport profiles for (a) a streamwise mode instability; (b) an oblique mode instability; and (c) a spanwise mode instability. $M_g = 5$.

the streamwise (a) and oblique (b) modes. The oblique mode also showed significant magnitudes for all components of the dissipation tensor whereas the streamwise and spanwise only displayed significant values for components along the streamwise and stream normal directions. The spanwise mode shows strong dissipation at the maximum shear locations.

The evolution of stream normal profiles for all terms of the RSEE have been investigated to complete this study on the influence of inhomogeneity in high-speed shear flows. The spanwise mode profiles exhibit a large constant energy production at regions of high shear and small magnitudes of pressure-strain and Reynolds stress flux. The streamwise and oblique modes present a gradual increase in their energy production profiles along with high magnitudes of pressure-strain redistribution and turbulent transport which aid in suppressing the perturbation growth. This final investigation provides explanation for the collective mode behavior shown in figure IV.5 where the high-speed Kolmogorov cases exhibit energies slightly higher than homogeneous shear flow, but still show the stabilizing influence of compressibility.

IV.E. Conclusions

The main objective of the present work is twofold i) provide supporting evidence that the modal stability boundaries seen in high-speed homogeneous shear and channel flows also exist in Kolmogorov flow, and ii) investigate and identify the qualitative influence of inhomogeneity on high-speed shear flows. The modal behavior in Kolmogorov flow is consistent with the previous studies. The subsonic modes, $\beta > \beta_{crit}$, are independent of initial Mach number and exhibit unstable growth. The

supersonic modes, $\beta < \beta_{crit}$, have stable growth and have strong dependence on the effective Mach numbers they experience. These results provide further credence to the hypothesis that all shear flows exhibit the same qualitative modal characteristics.

A comprehensive investigation on the evolution of individual stream normal planes is conducted to identify the effect of inhomogeneity in high-speed shear flows. The profile evolutions of the RSEE terms are studied to see determine the strength of interactions between stream normal planes with varying shear rates. The spanwise mode profiles displayed constant high production but small pressure redistribution and turbulent transport explaining the unstable growth of perturbations oriented along this direction. The streamwise and oblique modes exhibit varying production rates along with larger magnitude redistribution and transport terms, which leads to the perturbation growth suppression seen in the stable modal boundaries. These investigations explain the stabilizing influence of compressibility on Kolmogorov flow.

CHAPTER V

CONCLUSIONS AND FUTURE WORK

We perform three studies examining different effects on high-speed shear flows: (1) time-reversal properties of inviscid linear equations in incompressible and compressible flows; (2) a linear analysis investigation using rapid distortion theory to determine the influence of unsteadiness on a compressible periodic homogeneous shear flow field; and (3) a modal investigation on the effects of inhomogeneity in highly compressible shear flows. The contributions from each study are summarized:

V.A. Study 1

The concept of temporal flow reversal of the linearized invisicid equations is already established for incompressible flows. Using the same criteria, we examine time-reversal in compressible flows.

1 At the low-speed limit, the flow is governed by the Euler equation for momentum and the Poisson equation for pressure.

(a) In spectral space the Poisson equation becomes algebraic in form and can be substituted into the momentum equation to form a single governing equation of the flow field.

(b) Applying the time reversal transformation produces a sign change in the time derivative of the momentum equation exhibiting that low-speed linear, inviscid flow fields can be reversed.

2 At the high-speed or compressible limit, the governing equations include the mass, momentum and energy balance equations along with a state equation, here the ideal gas law, to properly capture the flow field. Applying time reversal transformation produces sign change of all ODE's in system proving high-speed linear, inviscid flow fields also are reversible.

V.B. Study 2

The characteristics of transition and turbulence in high-speed compressible periodic shear flows are remarkably different than constant shear flows. This is due to the vastly different pressure evolution in the periodic case compared to the constant shear case. In the constant shear case, the velocity field evolves through three distinct regimes where pressure's ability to counteract production changes in character. In the periodic shear case, the evolution of pressure becomes dependent on the periodic frequency.

1 For high frequency shear flows, the wave number vector remains almost constant in time preventing the pressure field - and simultaneously the velocity field - from evolving beyond its initial state.

2 For low frequency cases, the general solution of the inhomogeneous pressure equation obtains a form similar to the constant shear case but with coefficients and intermediate variables that are sinusoidal in nature. As a result, the early and late time limiting behavior can be surmised.

(a) The early time behavior produced the same result as the constant shear case: the transition between the first and second regime occurs at $S_0 t/\sqrt{M_m(t)} \approx 1$.

(b) At later times a coupling between the pressure and shear normal perturbation cause a drastic reduction in kinetic energy production similar to the second regime in steady flow.

(c) There is no point at which pressure evolves into the third regime found in the steady case.

The findings of this study have the potential to be used in unsteady compressible pressure strain correlation and Reynolds stress models. Since the majority of flow types experience some amount of time dependence, the inferences derived from this study could lead to possible control strategies to delay the onset of transition to turbulence. Further investigation of compressible unsteady flow fields need to be conducted.

V.C. Study 3

In this study we use DNS of Kolmogorov flow to i) examine the effects of inhomogeneity in a compressible shear flow and ii) exhibit the qualitative modal behavior seen in other shear flows is also present in a spatially periodic mean shear flow. Investigations of different modes lead to the following conclusions on the growth of fluctuations in high-speed inhomogeneous shear flows:

1 The modal behavior present in Kolmogorov flow is similar to the behavior identified in previous shear flow studies.

(a) Modes with $\beta > \beta_{crit}$ exhibit unstable growth that is independent of initial gradient Mach number which is consistent with subsonic flow.

(b) Modes with $\beta < \beta_{crit}$ exhibit dependence on their effective Mach number and smaller perturbation growth rates.

2 Examination of plane averaged turbulent quantities exposed a strong perturbation growth rate dependence on stream normal location illustrating that inhomogeneity in shear flows has a strong influence.

(a) Stream normal planes near maximum shear planes resemble homogeneous shear flow evolutions

(b) Planes in the vicinity of zero-shear display no growth at early times due to absence of production. Eventually perturbation growth occurs but only due to transport of energy from non-zero shear planes through turbulent transport and dissipation.

3 Evolutions of stream normal profiles of RSEE terms highlight the mechanisms responsible for varying perturbation evolution of the different modes.

(a) Modes with larger streamwise components develop time dependent production rates along the majority of the planes in the stream normal direction which has an influence on the evolution of the other RSEE terms, overall leading to a reduced perturbation growth rate.

(b) Modes with larger spanwise components maintain constant production rates coupled with pressure-strain and Reynolds flux terms that are an order smaller than the magnitudes of their streamwise counterparts.

REFERENCES

[1] P. Bradshaw. "Compressible turbulent shear layers." *Annual Review of Fluid Mechanics*, vol. 9, pp. 33-52,1977.

[2] S. Kline, B. Cantwell, G Lilley, U.S.A.F.O. S. Research, S.U.T.D.H. Transfer, and T. M. Program, *Complex Turbulent Flows: Computation, Experiment: the 1980-81 AFOSR-HTTM-Stanford Conference on Complex Turbulent Flows, Comparison of Computation and Experiment*. Thermosciences Division, Mechanical Engineering Department, Stanford University, 1982.

[3] D. Papamoschou and A. Roshko. "The compressible turbulent shear layer: an experimental study." *J. Fluid Mech.*, vol. 197, pp. 453-477, 1988.

[4] S. Sarkar."The stabilizing effect of compressibility in turbulent shear flow." *J. Fluid Mech.*, vol. 282, pp.163-186, 1995.

[5] A. Simone, G. N. Coleman and C. Cambon. "The effect of compressibility on turbulent shear flow: a rapid distortion theory and direct numerical simulation study." *J. Fluid Mech.*, vol. 330, pp. 307-338, 1997.

[6] T. Lavin, H. Yu and S. Girimaji. "Rapid distoriton analysis of compressible turbulence in ideal gas: Part 1-Reynolds averaged moments." *Bulletin of the American Physical Society*, 2006, retrieved from: `http://meetings.aps.org/link/BAPS.2006.DFD.AP.4`.

[7] S. Suman, H. Yu, and S. Girimaji. "Rapid distoriton analysis of compressible turbulence in ideal gas: Part 2-Density averaged moments." *Bulletin of the American Physical Society*, 2006, retrieved from: `http://meetings.aps.org/link/BAPS.2006.DFD.AP.5`.

[8] R. Bertsch and S. Girimaji. "Pressure effects in compressible flows at the rapid distortion limit." *Bulletin of the American Physical Society*, vol. 54, 2009, retrieved from:`http://meetings.aps.org/link/BAPS.2009.DFD.MB.10`.

[9] R. L. Bertsch, S. Suman and S.S. Girimaji. "Rapid distortion analysis of high Mach number homogeneous shear flows: Characterization of flow-thermodynamic interaction regimes." *Phys. Fluids*, vol. 24, no. 125106, pp. 1-24, 2012.

[10] T. A. Lavin, S. S. Girimaji, S. Suman and H. Yu, "Flow-thermodynamics interactions in rapidly-sheared compressible turbulence," *Theor. Comput. Fluid Dyn.*, vol. 26, pp. 501-522, 2011.

[11] G. Kumar, R. L. Bertsch & S. S. Girimaji, "Stabilizing action of pressure in high speed compressible shear flows: Effect of Mach number and obliqueness." *J. Fluid Mech.*, under review, 2014.

[12] Dazhi Yu and Sharath S. Girimaji. "Direct Numerical Simulations of homogeneous turbulence subject to periodic shear." *J. Fluid Mech.*, vol. 566, pp.117-151, 2006.

[13] S. S. Girimaji, J. R. O'Neill and D. Yu, "Rapid distortion analysis of homogeneous turbulence subjected to rotating shear." *Phys. Fluids*, vol. 8, no. 085102, pp.1-13, 2006.

[14] M. Duponcheel, P. Orlandi, and G. Winckelmans. "Time-reversibility of the Euler equations as a benchmark for energy conserving schemes." *J. Comp. Physics*, vol. 227, pp. 8736-8752, 2008.

[15] L. Fang, W. J. T. Bos, L. Shao, and J.-P. Bertoglio. "Time reversibility of Navier-Stokes turbulence and its implications for subgrid scale models." *J. Turbulence*, vol. 13, no. 3, pp. 1-14, 2012.

[16] H. Yu and S. S. Girimaji. "Extension of compressible ideal-gas RDT to general mean velocity gradients." *Phys. Fluids*, vol. 19, no. 041702, pp. 1-5, 2007.

[17] S. C. Kassinos and W. C. Reynolds. "A particle representation model for the deformation of homogeneous turbulence." *Annual Research Briefs*, Center for Turbulence Research, NASA Ames/Stanford University, pages 31-53, 1996.

[18] T. Lavin. *Reynolds and Favre-Averaged Rapid Distortion Theory for Compressible, Ideal Gas Turbulence*. A Master's Thesis. Department of Aerospace Engineering. College Station: Texas A & M University. 2007.

[19] S. S. Girimaji, E. Jeong and S. V. Poroseva. "Pressure-strain correlation in homogeneous anisotropic turbulence subject to rapid strain-dominated distortion." *Phys. Fluids*, vol.15, no. 10, pp. 3209-3222, 2003.

[20] D. Livescu and C. K. Madnia. "Small scale structure of homogeneous turbulent shear flow." *Phys. Fluids*, vol. 16, no. 8:2864-2876, 2004.

[21] C. Cambon, *Spectral study of an incompressible turbulent field, subject to coupled effects of deformation and rotation, externally imposed*, Doctoral Dissertation, France: University of Lyon, 1982.

[22] R. L. Bertsch, *Rapidly-Sheared Compressible Turbulence: Characterization of Different Pressure Regimes and Efect of Thermodynamic Flucuations*. M. S. Thesis. College Station: Texas A&M University. 2010.

[23] A.L. Frenkel. "Stability of an oscillating Kolmogorov flow." *Phys. Fluids A*, vol. 3, no. 7, pp.1718-1729, 1991.

[24] A. Thess. "Instabilities in two-dimensional spatially periodic flows Part II: Kolmogorov flow." *Phys. Fluids A*, vol. 4, no. 7, pp. 1385-1395, 1992.

[25] Y. Murikami and Y. Watanabe. "On Unstable modes of the Inviscid Kolmogorov Flow." *J. Physical Society of Japan*, vol. 63, no. 7, pp. 2825-2826, 1994.

[26] M.V. Ustinov. "Effect of a steady periodic velocity inhomogeneity on boundary layer stability." *Fluid Dynamics*, vol. 30, no. 4, pp. 523-529, 1995.

[27] I. Bena, M. Malek Mansour. "Hydrodynamic fluctuations in the Kolmogorov flow: Linear regime." *Physical Review E*, vol. 59, no. 5, pp. 5503-5510, 1999.

[28] V. Borue and S. A. Orszag. "Numerical study of three dimensional Kolmogorov flow at high Reynolds numbers." *J. Fluid Mech.*, vol. 306, pp. 293-323, 1996.

[29] J.V. Shebalin and S.L. Woodruff. "Kolmogorov flow in three dimensions." *Phys. Fluids*, vol. 9, no. 1, pp. 164-170, 1997.

[30] I. Bena, M. Malek Mansour. "Hydrodynamic fluctuations in the Kolmogorov flow: Nonlinear regime." *Physical Review E*, vol. 62, no. 5, pp. 6560-6570, 2000.

[31] A. Manela and J. Zhang. "The effect of compressibility on the stability of wall-bounded Kolmogorov flow." *J. Fluid Mech.*, vol. 694, pp. 29-49, 2012.

[32] K. Xu. "Gas kinetic schemes for unsteady compressible flow simulations." *VKI for Fluid Dynamics Lecture Series*, 1998.

[33] Kun Xu, "A Gas-Kinetic BGK scheme for the Navier-Stokes equations and its connection with artificial dissipation and Gogunov method." *J. Computational Physics*, vol. 171, pp. 289-335, 2001.

[34] K. Xu and M. Mao and L. Tang, "A multidimensional gas-kinetic BGK scheme for hypersonic viscous flow." *J. Computational Physics*, vol. 203, pp. 405-421, 2005.

[35] W. Liao, Y. Peng, and L.-S.Luo. "Gas-Kinetic schemes for direct numerical simulations of compressible homogeneous turbulence." *Physical Review E*, vol. 80, pp. 1-27, 2009.

[36] Kumar, G. Girimaji, S. S. and Kerimo, J. "WENO-enhanced gas-kinetic scheme for direct simulations of compressible transition and turbulence." *J. Computational Physics*,vol. 234, pp. 499-523, 2013.

[37] Kerimo, J. and Girimaji, S. S., "Boltzmann-BGK approach to simulating weakly compressible 3D turbulence: comparison between lattice Boltzmann and gas kinetic methods." *Journal of Turbulence*, vol. 8, no. 46, pp. 1-16, 2007.

[38] Yu, Huidan and Girimaji, S. S. and Luo, Li-Shi, "DNS and LES of decaying isotropic turbulence with and without frame rotation using lattice Boltzmann method." *J. Computational Physics*, vol. 209, no. 2, pp. 599-616, 2005.

[39] Lee, Kurnchul, *Heat release effects on decaying homogeneous compressible turbulence*. Doctoral Dissertation. College Station: Texas A&M University. 2008.

[40] Rogallo, R. S. "Numerical Experiments in Homogeneous Turbulence." *NASA Technical Memorandum*, 1981.

[41] Ristorcelli, J. R. and Blaisdell, G. A. "Consistent initial conditions for the DNS of compressible turbulence." *Physics of Fluids*, vol. 9, no. 1, pp. 4-6, 1997.

[42] Xie, Z. and Girimaji, S. S. "Linear Analysis and Direct Numerical Simulation of Small Perturbations in High-speed Channel Flow." *J. Fluid Mech.*, Under review, 2014.

[43] G. Kumar. *Modal analysis of instability, turbulence and novel control strategies in high mach number shear flows*. A Doctoral Dissertation. Department of Aerospace Engineering. College Station: Texas A & M University. 2012.

Supplemental Sources Consulted

[44] S. B. Pope *Turbulent Flows*. Cambridge University Press, 2000.

[45] M. J. Balmforth and Y. Young. "Stratified Kolmogorov Flow." *J. Fluid Mech.*, vol. 162, pp. 208232, 2002.

[46] M. J. Balmforth and Y. Young. "Stratified Kolmogorov Flow Part II." *J. Fluid Mech.*, vol. 528, pp. 23-42, 2005.

[47] G. Boffetta, et. Al. . "The viscoelastic Kolmogorov flow: eddy viscosity and linear stability." *J. Fluid Mech.*, vol. 523, pp. 161-170, 2005.

[48] B. Rollin, Y. Dubief and C. R. Doering. "Variations on Kolmogorov flow: turbulent energy dissipation and mean flow profiles." *J. Fluid Mech.*, vol. 670, pp. 204-213, 2011.

[49] G. K. Batchelor and I. Proudman. "The effect of rapid distortion of a fluid in turbulent motion." *Q. J. Mech. Appl. Math.*, vol. 7, pp. 121-152, 1954.

[50] C. Cambon, G. N. Coleman and D. N. N. Mansour. "Rapid distortion analysis and direct simulation of compressible homogeneous turbulence at finite Mach number." *J. Fluid Mech.*, vol. 257, pp. 641-665, 1993.

[51] G. Brethouwer. "The effect of rotation on rapidly sheared homogeneous turbulence and passive scalar transport, linear theory and direct numerical simulations." *J. Fluid Mech.*, vol. 542, pp. 305-342, 2005.

[52] P.A. Durbin and O. Zeman. "Rapid distortion theory for homogeneous compressed turbulence with application to modeling." *J. Fluid Mech.*, vol. 242, pp. 349-370, 1992.

[53] G. A. Blaisdell, G. N. Coleman and N. N. Mansour. "Rapid distortion theory for compressible homogeneous turbulence under isotropic mean strain." *Phys. Fluids*, vol. 8, no. 10, pp. 2692-2705, 1996.

[54] G. N. Coleman and N. N. Mansour. "Simulation and modeling of homogeneous compressible turbulence under isotropic mean compression." in *Turbulent Shear Flows 8*, pp. 269-282, Berlin:Springer-Verlag, 1993.

[55] L. Jacquin, C. Cambon and E. Blin. "Turbulence amplification by a shock wave and rapid distortion theory." *Phys. Fluids A*, vol. 5, no. 10, pp. 2539-2550, 1993.

[56] A. M. Savill. "Recent developments in rapid distortion theory." *Ann. Rev. Fluid Mech.* vol. 19, pp. 531-573, 1987.

[57] J. C. R. Hunt and D. J. Carruthers. "Rapid distortion theory and the 'problems' of turbulence." *J. Fluid Mech.*, vol. 212, pp. 497-532, 1990.

[58] S. S. Girimaji, J. R. O'Neil and D. Yu. "Rapid distortion analysis of homogeneous turbulence subjected to rotating shear." *Phys. Fluids*,vol. 18, no. 085102, pp. 1-13, 2006.

[59] G. N. Coleman and N. N. Mansour. "Modeling the rapid spherical compression of isotropic turbulence." *Phys. Fluids A*, vol. 3, pp. 2255, 1991.

[60] K XU and K. H. Prendergast. "Numerical Navier-Stokes solutions from gas kinetic theory." *J. Comp. Phys.*, vol. 114, pp. 9-17, 1994.

[61] P. L. Bhatnagar, E. P. Gross and M. Krook . "A model for collision processes in gases i. small amplitude processes in charged and neutral one-component systems." *Physical Review*, vol. 94, pp. 511-525, 1954.